Specific and comprehensive genetic targeting reveals brain-wide distribution and synaptic input patterns of GABAergic axo-axonic interneurons

Ricardo Raudales[1,2,#], Gukhan Kim[1], Sean M. Kelly, [1,2,&], Joshua Hatfield[1,3], Wuqiang Guan[1], Shengli Zhao[3], Anirban Paul[1,5], Yongjun Qian[1,3], Bo Li[1], Z. Josh Huang [1,3,4]

[1]Cold Spring Harbor Laboratory, Cold Spring Harbor, NY 11724, USA
[2]Program in Neurobiology, Stony Brook University, NY, 11794, USA
[3]Department of Neurobiology, Duke University, Durham, NC 27710, USA
[4]Department of Biomedical Engineering, Duke University, Durham, NC 27710, USA
[5]Department of Neural and Behavioral Sciences, Penn State College of Medicine, Hershey, PA, 17033

current affiliations: [#]Department of Psychiatry, Columbia University, 1051 Riverside Drive, NY; Division of Molecular Therapeutics, New York State Psychiatric Institute, 1051 Riverside 11 Drive, NY. [&]Department of Neurology, NYU School of Medicine, New York, NY 10016

*Correspondence to: josh.huang@duke.edu

Abstract

Axo-axonic cells (AACs), also called chandelier cells (ChCs) in the cerebral cortex, are the most distinctive type of GABAergic interneurons described in the neocortex, hippocampus, and basolateral amygdala (BLA). AACs selectively innervate glutamatergic projection neurons (PNs) at their axon initial segment (AIS), thus may exert decisive control over PN spiking and regulate PN functional ensembles. However, the brain-wide distribution, synaptic connectivity, and circuit function of AACs remains poorly understood, largely due to the lack of specific and reliable experimental tools. Here, we have established an intersectional genetic strategy that achieves specific and comprehensive targeting of AACs throughout the mouse brain based on their lineage (*Nkx2.1*) and molecular (*Unc5b*, *Pthlh*) markers. We discovered that AACs are deployed across essentially all the pallium-derived brain structures, including not only the dorsal pallium-derived neocortex and medial pallium-derived hippocampal formation, but also the lateral pallium-derived claustrum-insular complex, and the ventral pallium-derived extended amygdaloid complex and olfactory centers. AACs are also abundant in anterior olfactory nucleus, taenia tecta and lateral septum. AACs show characteristic variations in density across neocortical areas and layers and across subregions of the hippocampal formation. Neocortical AACs comprise multiple laminar subtypes with distinct dendritic and axonal arborization patterns. Retrograde monosynaptic tracing from AACs across neocortical, hippocampal and BLA regions reveal shared as well as distinct patterns of synaptic input. Specific and comprehensive targeting of AACs facilitates the study of their developmental genetic program and circuit function across brain structures, providing a ground truth platform for understanding the conservation and variation of a bona fide cell type across brain regions and species.

Introduction

The precision of inhibitory control is crucial for regulating information processing and routing in brain circuits (Roux & Buzsáki, 2015). In the cerebral cortex, inhibitory signaling is mediated by a large array of GABAergic interneurons (INs), which regulate the input and output of glutamatergic projection neurons (PNs), together forming dynamic ensembles of information processing and relay. Cortical INs comprise highly diverse subpopulations distinguished by their anatomical and physiological properties and gene expression profiles (Fishell & Kepecs, 2020; Gouwens et al., 2020; Huang & Paul, 2019; Tremblay et al., 2016). Recent single-cell RNAseq and computational analyses have delineated the hierarchical tree-like organization of cortical GABAergic neurons from subclasses and supertypes down to transcriptomic subtypes (Tasic et al., 2018)(BICCN 2021). Among these, the axo-axonic cells (AACs), or chandelier cells (ChCs), represent the most distinctive and a bona fide type, as they exclusively innervate the axon initial segments (AIS) of pyramidal neurons (PNs) (Somogyi, 1977; Somogyi et al., 1982). Because AIS are the site of action potential initiation and individual AACs innervate hundreds of PNs in their vicinity, AACs are thought to exert decisive control over spike generation in ensembles of PNs (Crick 1986) (Howard et al., 2005), thereby regulating network operations and information relay. Thus, a more complete understanding of AACs will not only provide key insights into the functional organization of cortical circuits but also facilitate an integrated multi-modal definition of ground truth neuron types, shedding light on the granularity of hierarchical cell type organization. However, current knowledge on AAC distribution, connectivity, and function remains incomplete, largely due to the lack of reliable experimental tools.

An ideal genetic tool for studying AACs, or any other bona fide neuron type, would have two important features: specificity (targeting only AACs but no other cells) and comprehensiveness or even completeness (capturing most if not all AACs). Genetic labeling of AACs was first achieved through fate mapping neural progenitors of the medial ganglionic eminence (MGE) at late embryonic stages using the *Nkx2.1-CreER* mouse line (Taniguchi et al., 2013). This approach has facilitated analyses of neocortical AAC subtypes (Wang et al., 2019), transcriptome profiles (Paul et al., 2017), connectivity (Lu et al., 2017), synapse development (Ishino et al., 2017; Tai et al., 2019), and activity-dependent pruning (Wang et al., 2021); it also enabled a comprehensive fate mapping of AACs across MGE neurogenesis (Kelly et al., 2019). However, late embryonic induction in *Nkx2.1-CreER* mice is not only cumbersome but also not entirely specific to AACs (Kelly et al., 2019), and does not capture all AACs. With the identification of several putative AAC molecular markers from scRNAseq datasets (Paul et al., 2017; Tasic et al., 2018), several gene-knockin driver lines have been generated, which have facilitated studying AACs. Yet, none of these driver lines have been shown to be specific and comprehensive. For example, the *Vipr2-ires-Cre* driver captures a subset of neocortical and basolateral amygdala (BLA) AACs, but is not entirely specific in these areas (Daigle et al., 2018; Nakashima et al., 2022; Tasic et al., 2018). Similarly, our *Unc5b-CreER* line enabled AAV targeting of hippocampal AACs, but also labels endothelial cells when combined with a reporter line (Dudok et al., 2021). Despite extensive effort to date, no singularly unique molecular marker for AACs has been identified. Indeed, the same is true for most if not all neuronal subtypes of the mammalian brain. Therefore, specific and comprehensive genetic access to ground truth neuron types remains a broad and major challenge in neural circuit studies.

Here, we leverage lineage origin and molecular markers to establish an intersectional strategy, achieving highly specific and comprehensive targeting of AACs across the mouse brain. We discovered that much beyond the neocortex, hippocampus and BLA as previously described, AACs are in fact widely distributed across all pallium-derived brain structures and beyond. These include not only the dorsal pallium-derived neocortex and medial pallium-derived hippocampal formation, but also the lateral pallium-derived claustrum-insular complex, the ventral pallium-derived extended amygdaloid complex, and olfactory centers such as piriform cortex. In addition, putative AACs are also abundant in anterior olfactory nucleus, taenia tecta and are also found in the lateral septum and the diencephalic or third-ventricle-derived hypothalamus. The comprehensive labeling of cortical AACs allowed us to quantify their areal, laminar, and axon terminal distribution as well as to describe multiple anatomic subtypes. We further extend our strategy to AAV-based targeting and map synaptic input sources to AACs in sensorimotor cortical areas, hippocampal CA1, and BLA, demonstrating feasibility for functional manipulations. Together, these results provide a brain-wide overview of AACs and their subtype variations and input sources in the cerebral cortex. Precise and comprehensive genetic access to AACs sets the stage for understanding many aspects of their role in circuit development and function across the extended brain regions. This establishes a powerful model system to study the conservation and divergence of a ground truth neuron type across different brain regions towards understanding the principles of cell type organization.

Results

Lineage and marker-based intersectional targeting captures AACs across brain regions

The embryonic subpallium generates GABAergic neurons of the telencephalon, with the medial ganglionic eminence (MGE) giving rise to AACs (Kelly et al., 2019; Taniguchi et al., 2013) while other progenitor domains, such as the caudal ganglionic eminence (Miyoshi et al., 2015) or preoptic area (Gelman et al., 2011) do not. Within the MGE *Nkx2.1* lineage, AACs are generated in two consecutive waves during both early and late neurogenesis (Kelly et al., 2019), extending our initial report of their birth pattern (Taniguchi et al., 2013). Therefore, late embryonic induction in the *Nkx2.1-CreER* line only enriches a subset of neocortical AACs and also labels at least two other interneuron types (Kelly et al., 2019); this strategy also misses AACs in the hippocampus, BLA, and potentially other brain areas that are born earlier (Kelly et al. 2019). Taking a different approach based on scRNAseq analysis, we identified several putative AAC markers (Paul et al., 2017) and accordingly generated *Unc5b-CreER* and *Pthlh-Flp* driver lines. However, neither by itself is fully specific to AACs: the former also labels endothelial cells and sparse cortical pyramidal neurons (data not shown), and the latter labels a subset of CGE-derived interneurons (Figure 1—figure supplement 3m-p). To purify AACs from these driver lines, we then designed an intersectional strategy that combines lineage and molecular markers (Figure 1a); we tested the intersection of *Nkx2.1-Flp* with *Unc5b-CreER* as well as *Nkx2.1-Cre* with *Pthlh-Flp*. We expected that the constitutive *Nkx2.1-Flp* or *Cre* line would cover the entire output from MGE, including all AACs, and the intersection with postmitotic markers would specifically capture AACs.

We first combined *Nkx2.1-Flp* and *Unc5b-CreER* driver lines with an *Ai65* intersectional reporter allele to generate *Unc5b-CreER;Nkx2.1-Flp;Ai65* mice (Figure 1b). Tamoxifen induction (TM) allows dose-dependent titration of AAC labeling density, allowing the characterization of global

distribution patterns *en masse* with high dose as well as the evaluation of individual cell morphologies with sparser labeling by lower dose (see methods). Indeed, postnatal high dose TM induction generated dense and highly characteristic AAC labeling patterns throughout the neocortex, hippocampus, and BLA (Figure 1d-g). The characteristic chandelier axon arbor morphology with strings of synaptic boutons ("cartridges") along the AIS of pyramidal neurons unequivocally indicated their AAC identity (Figure 1, Figure 1—figure supplement 1-3).

Surprisingly, cell labeling extended much beyond these three previously reported structures that contain AACs. As the AAC identity of labeled cell are validated in most but not all these structures, we tentatively call some of these putative AACs (pAACs). Extensive analysis of these brain regions revealed an overarching pattern: AACs and pAACs are abundantly present in essentially all pallium-derived structures and several additional structures (Table 1; Figures 1c-g, Figure 1—figure supplement 1-2, Supplemental movie 1). The dorsal pallium (dPAL)-derived structures include the entire neocortex and entorhinal/ectorhinal cortices. The medial pallium (mPAL)-derived structures include the entire hippocampal formation. Beyond these previously known structures, pAACs are abundant in lateral pallium (lPAL)-derived claustrum, insular, and endopiriform dorsal. In addition, the ventral pallium (vPAL)-derived structures include most of the amygdaloid complex (cortical amygdala, basolateral and basomedial amygdala, and medial amygdala) and extended amygdala (bed nucleus of stria terminalis). Most surprisingly, AACs are highly abundant in a set of olfactory centers including piriform cortex, anterior olfactory nucleus, and taenia tecta. Among these, the piriform derives from the vPAL while AON and TTd derive from septum neuroepithelium. Finally, pAACs are found in lateral septum (also derived from septum neuroepithelium (Magno et al., 2022) and parts of the hypothalamus (derived largely from neuroepithelium of the third ventricle).

Consistent with these findings, the *Pthlh-Flp;Nkx2.1-Cre;Ai65* mice were found to have a similar overall pattern of pAAC distribution across different brain regions, with several differences (Figure 1—figure supplement 3). First, this intersection also labeled a set of layer 4 interneurons in the somatosensory cortex (Figure 1—figure supplement 3f). Second, *Pthlh;Nkx2.1* yielded slightly higher cell targeting in retrosplenial cortex (Figure 1—figure supplement 3h-i). Third, *Pthlh;Nkx2.1* labelled fewer cells in the AON and BST). As an additional application of the *Pthlh-Flp* line, we demonstrate that when combined with an inducible *Nkx2.1-CreER* driver (Taniguchi et al., 2013) the *Pthlh-Flp;Nkx2.1-CreER;Ai65* mice led to exclusive fate mapping of AACs (Figure 1—figure supplement 3j-l). The overall similarity between *Unc5b/Nkx2.1* and *Pthlh/Nkx2.1* patterns, and high density of cells captured, provided independent evidence that these intersectional approaches may have captured most if not all AACs in the brain.

In addition to targeting AACs, the *Pthlh-Flp* is a useful tool for at least two additional cell types. First, consistent with its expression in a set of CGE-derived interneurons (including VIP-expressing cells), intersection with the *VIP-Cre* driver line, which alone expresses in other cell types, was highly-specific for an interneuron subtype with striking vertical morphology that may represent interneuron-selective cells (Figure 1—figure supplement 3m-p). Second, *Pthlh/Nkx2.1* intersection yielded dense labeling of striatal interneurons (i.e. striatal neurons without axons in SNr/GPi)

186 (Figure 1—figure supplement 3f-h), consistent with known *Pthlh* expression in striatal PV
187 interneurons (Munoz-Manchado et al., 2018).
188
189 In sum, our lineage and marker intersections combining *Nkx2.1- Flp/Cre,* or *CreER* with *Unc5b-*
190 *CreER* or *Pthlh-Flp* appear to have achieved unprecedented specificity and comprehensiveness of
191 AAC targeting. To validate this result, in the following sections, we present more detailed and
192 quantitative descriptions of AACs and pAACs across brain structures.
193
194 **Areal, laminar, and subtype distribution of AACs across the neocortex**
195 Previous studies have identified ChCs in multiple neocortical areas and cortical layers with the
196 observation of several morphological variants (Kelly et al., 2019; Somogyi et al., 1982; Taniguchi et
197 al., 2013; Wang et al., 2019), but the global and quantitative distribution of ChC across the cerebral
198 cortex and cortical layers is unknown. To first validate the specificity of our method to ChCs, we
199 used single low dose TM induction to sparsely label individual cells across cortical areas (Figure 2—
200 figure supplement 1). Combined with immunolabeling of AnkyrinG-stained pyramidal neuron (PN)
201 AIS, we showed that the vast majority of RFP^+ cells (97.3%, n=110 cells from 6 mice) had axonal
202 cartridge structure with synaptic boutons along PN AIS, validating their ChC identity (Figure 2—
203 figure supplement 1).
204
205 To systematically map and quantify ChC distribution across the entire cerebral cortex, we then used
206 high dose TM induction in *Unc5b-CreER;Nkx2.1-Flp;Ai65* mice to densely label ChCs and
207 performed serial 2-photon tomography (STP) across the entire mouse brain at 50um intervals
208 (Supplemental movie 1). The whole brain STP datasets were then registered to the Allen CCFv3
209 atlas, followed by segmentation of anatomical regions and an automated cell detection algorithm was
210 applied to identify and quantify labeled cells in each region (Ragan et al., 2012; Kim et al., 2017;
211 Matho et al., 2021). ChCs were detected across all areas of cerebral cortex (Figure 2a; Supplemental
212 movie 1). Normalized cell density analysis revealed area-specific patterns (Figure 2b). The highest
213 densities were observed in ventrolateral areas such as PERI, ECT, TEA, and AI as well as
214 ventromedially in ILA (see appendix for abbreviations). There was a slight decline in ChC density
215 very rostrally in FRP or caudally in RSP.
216
217 We further mapped ChC distribution across cortical layers in several sensory and motor areas
218 (Figure 2c, d). The majority of ChC somas were located in L2/3, though this was area specific, with
219 normalized density ranging from the lowest in SSs (65.5±0.6%) to highest in VISp (94.7±1.0%). An
220 analysis of relative cortical depth (Figure 2e) revealed that ~80% of ChCs occupied a narrow band
221 just below the L1/2 border, though this varied by anterior-posterior location. Nevertheless, ChCs
222 were found at nearly all cortical depths, with a sizable proportion forming a second, less dense band
223 above the white matter tract. This largely "bilaminar" pattern was highly evident in certain areas
224 such as the SSp (Figure 2f).
225
226 To more systematically sample the morphological variations of ChCs, we used low dose TM
227 induction to resolve individual cells across areas (Figure 2—figure supplement 1). We identified all
228 the previously described laminar and morphological subtypes (Wang 2019), including supragranular

229 (L2/3) (Figure 2g), infragranular (L5/6) (Figure 2h), and inverted (axon arbors extend above cell
230 soma). Notably, we found rather frequent bi-laminar and tri-laminar subtypes–L2/3 ChCs extending
231 their axon arbors not only locally but further down to another one or two deep layers (Figure 2i).
232 These translaminar ChCs may coordinate PN ensembles between cortical layers. The abundance of
233 translaminar ChCs varied among cortical areas, e.g. with high abundance in auditory cortex (Figure
234 2j).
235
236 In addition to soma position and cell morphology, we sought to map the distribution of ChC axon
237 terminals (i.e. cartridges) throughout the mouse cortex. For this purpose, we used a Cre/Flp-
238 dependent reporter line expressing a synaptophysin-EGFP fusion protein and cytoplasmic tdTomato
239 (Niederkofler et al., 2016) (Figure 2k-l). Following high-dose induction and dense labeling, we
240 performed whole brain STP imaging and calculated cartridge density across ARAv3 areas (see
241 Methods). ChC cartridges exhibited a wide range of densities across areas and layers (Figure 2m),
242 with overall similarity to ChC soma densities in those areas and layers (Figure 2b). Plotting the
243 relative laminar depth for ChC cartridges in each area (Figure 2n) revealed characteristic patterns of
244 population-level laminar innervation onto PNs.
245
246 **AACs in the hippocampus**
247 Decades of studies of hippocampal AACs using traditional anatomical and physiological methods
248 have implicated their role in network oscillations, including sharp waves and epilepsy (Fitzgerald et
249 al., 2013; Klausberger et al., 2003; Viney et al., 2013) but the quantitative distribution of AACs
250 across hippocampal formation has remained unknown, and reliable genetic access to hippocampal
251 ACCs is not well established. We applied *Unc5b/Nkx2.1* intersectional targeting and STP to map
252 AAC distribution throughout hippocampal compartments. Single cell labeling by low-dose
253 tamoxifen and immunohistochemistry confirmed that the vast majority (98.2%, n=56 cells, 6 mice)
254 were AACs, characterized by vertically-oriented cross laminar apical dendrites in CA1-CA3 and
255 axon terminals innervating PN AIS (Figure 3a-b, d). Dense labeling with high dose TM followed by
256 cell density analysis revealed that AAC density was, surprisingly, highest in CA2 and lowest in
257 dentate gyrus (Figure 3c), with density in CA1 and CA3 approximately equal. Only a very sparse
258 population of AAC was labelled in dentate gyrus. Overall AAC density in CA2 was 3-4 fold greater
259 than CA1/CA3 and 13-fold greater than DG (Figure 3c). As the density of PNs across hippocampal
260 areas are overall similar, this result suggests substantially different AAC-PN innervation ratio and
261 that AACs may exert much denser and likely stronger control of CA2 PNs than CA1/CA3 PNs or
262 DG granule cells.
263
264 **AACs in anterior insular, claustrum, and dorsal endopiriform nuclei**
265 According to the updated tetrapartite model of pallial/cortical development (Figure 1c), the lateral
266 pallium gives rise to the claustro-insular complex as well as the dorsal endopiriform nuclei (EPd)
267 (Puelles, 2017). Our brain wide imaging of *Unc5b-CreER;Nkx2.1-Flp;Ai65* mice revealed pAACs
268 deployed across these three regions (Figure 4a). Unlike cortical and hippocampal AACs whose axon
269 arbors exhibit highly characteristic laminar pattern, reflecting the organization of their postsynaptic
270 targets (i.e. AIS of PNs), the axon arbors of RFP cells in AI, CLA, EPd do not show clear laminar
271 patterns and exhibit less uniformity and are more multipolar in morphology (Fig 4b-c), making it

272 more difficult to ascertain their identity. Nevertheless, strings of synaptic boutons were frequently
273 identified that co-localized with AnkG labeled AIS, suggesting these as pAACs. Quantification from
274 dense labeling revealed higher pAAC density in EPd compared to claustrum and EPv, the latter of
275 which structure is derived from ventral pallium (Figure 4d).
276
277 **AACs in the amygdaloid complex and extended amygdala**
278 The amygdaloid complex includes over a dozen nuclei and can be segregated into 5 groups (Beyeler
279 & Dabrowska, 2020): 1) the basolateral amygdala (BLA) divided into a dorsal section (lateral
280 amygdala, LA) and basal section (basal amygdala, BA), 2) the basomedial amygdala (BMA), 3) the
281 central amygdala (CeA) further splits into medial, lateral, and central sections (CeM, CeL, and CeC),
282 4) the medial amygdala (MeA), and 5) the cortical amygdala (CoA). Furthermore, the CeM extends
283 rostrally and medially, thereby including the bed nucleus of stria terminalis (BST) to form the
284 extended amygdala. Based on developmental origin, connectivity, and gene expression, these
285 groups can be assigned into two large categories: pallium-derived cortex-like structures and
286 subpallium-derived basal ganglia-like structures. The former includes BLA, CoA, BMA, and MeA,
287 while the latter includes CeA and BST. Within the amygdala nuclei, projection neurons are
288 exclusively glutamatergic in BLA, CoA, BMA, exclusively GABAergic in CeA, and predominantly
289 GABAergic in MeA and BST. In rodents, there is also a population of GLU PNs (derived from third
290 ventricle neuroepithelium) that populates the BST, MeA, and hypothalamus (Garcia-Moreno et al.,
291 2010; Huilgol and Tole, 2016).
292
293 In this context, we found AACs or pACCs in all the amygdala nuclei containing GLU PNs, i.e.
294 except CeA (Figure 4i-h). Sparse labelling and immunohistochemical co-staining with AnkG
295 confirmed that the labeled cells in these compartments were nearly exclusively AIS-targeting (97.2%,
296 n=36 cells, 6 mice). Morphologically, AACs in the amygdala tended to be similar to those in the
297 claustrum, exhibiting multipolar dendrites and multipolar axon terminal branches (in contrast to
298 axon arbor of cortical AACs that typically extend either below or above the soma) (Figure 4f). The
299 density of AACs in amygdala appears to correlate with the known abundance of GLU PNs: densities
300 in BLA, CoA, BMA were much higher than those in MeA and BST. Among the pallium-derived
301 amygdala subdivisions (LA, BLA, BMA, PA), AACs were present at roughly similar densities
302 (Figure 4i), while among striatum-like amygdala nuclei they were largely concentrated in MeA
303 (Figure 4j). Our results indicate that AACs are deployed to all amygdala nuclei containing GLU
304 PNs. Within the largely GABAergic structures such as MeA and BST, we hypothesize that pAACs
305 might innervate the minor glutamatergic PNs in these structures.
306
307 **AACs in olfactory centers: piriform cortex, AON, TTd**
308 A major novel finding is the surprising abundance of ACCs across multiple olfactory centers.
309 Derived from the ventral pallium, the piriform cortex had been reported to contain axo-axonic
310 synapses by co-localization of the inhibitory presynaptic marker GAT1 and AnkG (Wang and Sun,
311 2012). Our dense labelling in *Unc5b-CreER;Nkx2.1-Flp;Ai65* mice revealed a striking abundance of
312 AACs that span the anterior-medial extent of the piriform in a single layer (Figure 5a-c). Sparse
313 labeled single AACs exhibited characteristic morphologies analogous to L2/3 AACs of the
314 neocortex, with extended branching of apical dendrites to L1 and dense axon arbors below the cell

body forming cartridges along PN AIS (Figure 5d-j). The single layer distribution pattern of piriform AACs continued dorsally to the insular cortex and ventrally to piriform-amygdala area (PAA) and COA (Figure 5c).

Furthermore, we found that AACs are deployed to two other olfactory centers that derive from outside of the four pallial domains: namely the anterior olfactory nucleus (AON) and taenia tecta (TT) (Figure 6a-b). Though exhibiting a range of different morphologies, AACs in all three areas resemble those of L2/3 neocortex, with apical dendrites often extending to the pia and basally-oriented axon arbors; their somata are located at the upper border of the pyramidal cell layer in the case of TT and AON (Figure 6c-g). Overall, AACs in piriform, TT, and AON exhibited higher density than AACs in cortex, hippocampus, and amygdala (Figure 6h, see Extended Data for Figures 2, 3, and 6).

AACs in the lateral septum

The LS, despite having no distinct laminar structure (delineated in ARAv3), shows some evidence of differential mRNA expression in superficial and deep domains, possibly analogous to a laminar organization (Besnard and Leroy, 2022). In *Unc5b-CreER;Nkx2.1-Flp;Ai65*mice, AACs tended to locate towards the midline (Figure 6b). Individual AACs were morphologically similar to cortical AACs, with extensive apical dendrites extending toward the midline and axon arbors and cartridges typically protruding away and into the cellular layer (Figure 6i-k).

Monosynaptic input tracing to AACs in sensorimotor cortex

In addition to using Cre AND Flp-dependent reporter lines for AAC access, it is advantageous to extend our intersectional strategy to engage viral vectors that enable more selective and anatomy-based labeling, recording, and manipulation. Because the endogenous expression of *Unc5b* and *Nkx2.1* occur at non-overlapping stages in development, it is not feasible to directly use Cre-AND-Flp dependent viral vectors (Fenno et al., 2020). Instead, we crossed *Unc5b-CreER;Nkx2.1-Flp* driver with a Cre-AND-Flp dependent tTA2 reporter line (Figure 7a) (Matho et al., 2021), which provides an indelible genetic handle for delivery of tTA-activated viral reporters. We tested this approach in AACs to map their synaptic input source by using tTA-activated AAVs in of *Unc5b-Cre;Nkx2.1-Flp;dual-tTA2* mice (Figure 7b; Figure 7 – Figure supplement 1b, c). We used the PV cell (PVC) population for comparison largely due to convenience, recognizing the fact that PVCs also include some ChCs.

We crossed the *dual-tTA2* reporter to either *Unc5b-CreER; Nkx2.1-Flp* or *PV-Cre; Nkx2.1-Flp* and performed monosynaptic input tracing to ChCs and PV cells (PVCs), respectively, in three sensorimotor areas: MOs, MOp, and SSp (Figure 7a-c, Figure 7 – Figure supplement 1a). Intersecting *PV-Cre* with *Nkx2.1-Flp* is a strategy for specifically targeting PV interneurons, as *PV-Cre* also captures a sparse population of excitatory pyramidal neurons (van brederode et al., 1991). Although PV is expressed in up to ~50% of cortical ChCs, starter cell depth distribution was found to be largely non-overlapping between injected ChCs and PVCs, likely due to the much higher abundance of PV basket cells (Figure 7d, Figure 7 – Figure supplement 1d-e).

358 Across sensorimotor cortex ChCs and PVCs integrated into highly-interconnected cortical networks.
359 $ChCs^{MOs}$ received ~50% of inputs from motor areas (41.0±2.3% in MOp, 4.5±0.7% in contra MOs)
360 followed by SSp (20.4±4.2%) and SSs (9.5±0.7%) (Figure 7e). Long-range inputs to $ChCs^{MOp}$ were
361 largely dominated by sensory cortex (63.2±11.3% in SSp, 10.1±1.3% in SSs), followed by MOs
362 (12.7±6.7%) and contra MOp (4.2±2.5%) (Figure 7f). In contrast, $ChCs^{SSp}$ received only ~65%
363 inputs total from sensorimotor (42.2±0.5% in SSs, 11.1±1.2% in MOs, 7.8±1.9% in MOp, 3.03±0.2%
364 in contra SSp), with considerably more inputs from thalamus and other cortical areas (Figure 7g).
365 Thalamocortical (TC) afferents to $ChCs^{MOs}$ and $ChCs^{MOp}$ were primarily from VAL, whereas TC
366 inputs to $ChCs^{SSp}$ were mostly from VPM. In addition to sensorimotor, other cortical areas such as
367 ORB, FRP, AI, VIS, ACA, RSP, and AUD comprised a minor source of long-range inputs.
368 Interestingly, we identified sparse inputs from GPe directly to ChCs and PV in all three cortical
369 areas. Overall input patterns were comparable between ChCs and PV, although ChCs received
370 significantly less homotypic inputs from the contralateral hemisphere for each injection site (Figure
371 7e-g).
372
373 **Monosynaptic input tracing to AACs in CA1**
374 The functional role of AACs is perhaps best understood in hippocampus, where CA3 AACs tend to
375 fire at distinct epochs compared to other cell types and near the peak of theta oscillations (Viney et
376 al., 2013). Little is known about the inputs to AACs that might drive this cell-type functional
377 distinction, although non-specific tracers have identified an inhibitory connection from medial
378 septum (MS) to AACs in CA3 (Viney et al., 2013). More recently, we used *Unc5b-CreER* to
379 functionally characterize the firing patterns of $AACs^{CA1}$ during whisking and locomotion (Dudok et
380 al., 2021). Here, we applied cell type targeted retrograde monosynaptic tracing to map long-range
381 inputs to $AACs^{CA1}$ (Figure 8a-b).
382
383 Compared to cortical ChCs, $AACs^{CA1}$ received inputs from more diverse sets of sources. Within the
384 hippocampus formation, $AACs^{CA1}$ received asymmetric inputs from each hemisphere, with relatively
385 a higher fraction in CA3 contralaterally (29.0±2.4%) but higher ipsilaterally in DG (4.3±1.5%) and
386 ENT (11.6±3.6%) and SUB (15.2±5.2%) (Figure 8c). Surprisingly, while the aforementioned study
387 (Viney et al., 2013) found inhibitory connections from MS to AACs in CA3, we found in $AACs^{CA1}$
388 over two-fold higher input connectivity from adjacent NDB (5.1±0.9%) compared to MS (2.0±0.2%).
389 (Figure 8d-e). Immunohistochemistry analysis found the majority of these long-range inputs were
390 inhibitory (56.8±4.8%) and a sizeable proportion ChAT-positive (27.6±4.0%) (Figure 8f-j).
391 $AACs^{CA1}$ also received diverse cortical inputs, including from VIS, RSP, AUD, SSp, PTLp, SSs,
392 Tea, and PERI, as well as TC afferents from ATN (Figure 8l-p; see abbreviations in appendix).
393
394 **Monosynaptic input tracing to AACs in basolateral amygdala**
395 Comparatively little is known about the function or circuit role of $AACs^{BLA}$. Past studies have had to
396 largely rely on post hoc identification from paired recordings, demonstrating their potent inhibitory
397 effects (Veres et al., 2014). However, without cell type-specific tools for $AACs^{BLA}$, the long-range
398 afferent connectivity that might drive these effects has remained virtually unknown. We applied our
399 intersectional targeted approach to reveal the monosynaptic inputs to $AACs^{BLA}$ (Figure 9a-b).
400 $AACs^{BLA}$ received highly diverse sets of inputs (Figure 9c). $AACs^{BLA}$ received strongest afferents

401 from PIR (13.1±1.1%) and the hippocampal-entorhinal network (ENT 12.7±0.2%, CA1 10.5±2.0%,
402 SUB 8.0±0.1%) (Figure 9e, h-i). The next strongest inputs originated from cortical amygdala areas
403 (TR, PAA, COA) and cortical subplate nuclei (CeA, LA, EP, BMA) (Figure 9d). TC afferents were
404 largely from MTN (2.6±0.4%), while cortical projections were identified in AI, AUD, PERI, ECT
405 (Figure 9f). Input cells in LZ and MEZ of hypothalamus were found to be glutamatergic, while those
406 from GPe and EP were GABAergic (Figure 9j-o).
407
408 **Discussion**
409
410 **Specific and comprehensive targeting of ground truth cell types**
411 A major challenge in studying the functional organization of GABAergic inhibitory circuits, and
412 neural circuits in general, is establishing specific and comprehensive genetic access to ground truth
413 cell types. Here, leveraging an intersectional strategy that integrates lineage and molecular markers,
414 we have achieved near-perfect specificity and near-complete comprehensiveness in targeting a bona
415 fide interneuron type. This strategy will facilitate studying the connectivity, function, and
416 development of AACs across brain regions, thereby providing a robust experimental platform for
417 integrating multi-modal analysis of a ground truth cell type across brain circuits. A practical
418 drawback of this approach is the requirement of combining three engineered genetic alleles. In this
419 context, the *Unc5b-CreER* line by itself is already useful for AAV-mediated targeting of AACs
420 (Dudok et al., 2021). Because most AAVs are neurotrophic, Cre-activated AAVs would bypass
421 endothelial cells to target only AACs in the *Unc5b-CreER* line, even though this approach is not
422 suited to quantify brain-wide AAC patterns. Beyond relying on germline engineering, the recently
423 invented CellREADR technology (Qian et al., 2022) will further simplify AAC targeting by
424 identifying an RNA sensor of *Unc5b* mRNA and deliver it with an AAV vector. As *Unc5b* is a
425 conserved AAC marker from rodents to primates including humans, the CellREADR approach may
426 enable genetic access to AACs across mammalian species.
427
428 **Implications of brain-wide AAC distribution pattern**
429 The initial discovery of neocortical AACs was based on their striking chandelier-like morphology
430 (Szentágothai, 1975), reflecting the spatial arrangement of their exclusive synaptic targets – the AIS
431 of cortical pyramidal neurons (Somogyi, 1977; Somogyi et al., 1982). This defining feature of
432 synapse specificity led to subsequent discoveries of AACs in the hippocampus and BLA. These
433 findings have relied on meticulous efforts of skilled neuroanatomists to correctly identify AACs,
434 mostly post hoc, by synapse specificity at AIS (Bienvenu et al., 2012; Veres et al., 2014). Since then,
435 it has been widely assumed that AACs are restricted to these brain structures, and likely to the
436 mammalian species. Here, based on developmental lineage and key molecular markers that likely
437 include all AACs, our results reveal a vastly expanded and likely complete brain distribution pattern
438 of AACs. Most importantly, we found that pAACs are deployed to the entire pallium-derived brain
439 structures (Puelles, 2017), including not only the dPAL-derived neocortex and mPAL-derived
440 hippocampal formation, but also the lPAL-derived claustrum-insular complex, the vPAL-derived
441 extended amygdaloid complex, piriform cortex, and other olfactory centers such as AON, taenia
442 tecta. In addition, subregions of the lateral septum and hypothalamus also contain pAACs.
443
444 Among the pallium-derived structures, the density of AACs vary substantially within and across
445 regions. For example, within the neocortex, ChCs are highest in perirhinal and lowest in

retrosplenial cortex. Across cortical layers, AACs are highly concentrated in L2, enriched in L5/6, and significantly less abundant in middle layers. Consistent with these results, the number and density of GABAergic synapses at AIS also vary substantially among different PyNs within and across cortical layers (DeFelipe et al., 1985; Fish et al., 2013; Schneider-Mizell et al., 2021). Similar variations are seen across the hippocampal formation, where CA2 exhibit the highest and DG the lowest density. It is also possible that these regional differences might reflect the distinction of PN types and/or their inherent physiological and connectivity properties that might require different levels and ratio of AAC control.

In particular, the finding of a striking abundance of AACs in olfactory centers across piriform cortex, AON, taenia tecta suggests strong inhibitory regulation of PNs at AIS in these regions. Although the functional significance is not yet clear, the simpler circuit architecture and strong link to innate rodent behaviors of these olfactory centers may facilitate uncovering the logic of AAC function. Furthermore, as these olfactory circuits are evolutionarily preserved across vertebrate species (Zeppilli et al., 2023), our finding raises the possibility that AACs might be present in the CNS of other vertebrates, beyond the mammalian brain.

Notably, although the MeA and BST comprise mostly GABAergic neurons that are primarily generated from the subpallium, they contain subsets of glutamatergic projection neuron that migrate from pallium origin (Beyeler & Dabrowska, 2020) or from the third ventricle (Garcia-Moreno et al., 2010). The true AAC identity in these regions, and in several other regions such as the hypothalamus, remains to be validated by synapse innervation at AIS of GLU PNs. Nevertheless, based on current results, our overarching hypothesis is that AACs are deployed across all pallium-derived structures to control the AIS of GLU PNs, including those in MeA and BST. Our results also indicate that AACs are absent from the rest of the CNS. This finding suggests a major distinction between the physiology and functional organization of pallium-derived GLU PNs versus those in other CNS regions.

AACs as a model for understanding neuronal cell type organization across regions and species

The rapid scaling of single cell RNA sequencing enables the generation of massive transcriptome datasets across brain regions and species (Trygve E. Bakken et al., 2021; Hain et al., 2022). These datasets provide unprecedented opportunities to discover the organization and relationship of cell types within and across brain regions, which reflect their gene regulatory programs and developmental origin. Cross species analyses promise to further reveal the evolutionary conservation and divergence of brain cell types (T. E. Bakken et al., 2021; Tosches, 2021). However, transcriptomic cell homologies between brain regions and species, especially more distantly related regions and species, are often discernible only at a relatively coarse level and do not fully capture the biological complexity (Tosches, 2021). A major challenge is to evaluate statistically defined transcriptomic similarity against biological ground truth, such as anatomic connectivity and developmental relationship. In this context, the most appealing attribute of AACs is their singularly defining synapse specificity at AIS of GLU PNs, which can be readily measured and validated. Under this overarching connectivity-based definition, all other molecular and phenotypic variations can be assessed and organized accordingly regardless of brain regions and species. Therefore, genetic access to AACs across brain regions provides a rare and compelling ground truth platform that can unambiguously identify this cell type across regions and species. This will further facilitate transcriptomic and epigenomic analysis to discover the gene regulatory program of AACs, and

contribute to understanding the principles of cell type organization by linking developmental genetic program, circuit connectivity and function, and evolutionary trajectory.

Acknowledgements

We thank P. Wu for generating the *Unc5b-CreER* and *Pthlh-Flp* mouse lines, R. Drewes for extensive support with STP imaging, K. Matho for help with cell detection and image analysis, S. George and L.Van Aelst for helpful discussions and providing antibodies, and S. Suryanarayana and D. Huilgol for extensive discussion and critical reading of the manuscript. We thank CSHL Animal Resources for mouse husbandry and Salk for providing rabies virus. This work was supported in part by the NIH grants 5R01MH094705-10, 5R01MH109665-05, and 5DP1MH129954-02 to Z.J.H; 5R01MH101214-08 and 2R01MH108924-06 to B.Li; and by the CSHL Robertson to Z.J.H. R.R. was supported by the NRSA F31 Predoctoral Fellowship 5F31MH114529-03 and A.P. by a NARSAD Post-doctoral Fellowship.

Author Contributions

Z.J.H. and B.L. conceived the study and obtained funding. Z.J.H. coordinated the study. Z.J.H., B.L., and R.R. designed the experiments. R.R., G. K., S.K., A.P., J.H., and S.Z. conducted mouse breeding, anatomy, immunohistochemistry, imaging and quantification. R.R. and W.G. performed virus injection experiments. R.R. and J.H. conducted whole-brain STP tomography and analysis of cell distribution patterns. S.Z. performed HCR ISH experiments. R.R. and Y.Q. generated the starter AAV virus. Z.J.H. and R.R. wrote the manuscript with contributions and edits from B.L. and S.K.

531 **Figure Legends**

532 **Figure 1. Developmental genetic intersectional targeting reveals brain-wide AAC distribution**
533 **patterns.**

534 a) Schematic of lineage (*Nkx2.1*) and marker (*Unc5b*) intersection for pan-AAC labeling. Embryonic
535 *Nkx2.1* expression defines MGE interneuron identity while subsequent postnatal *Unc5b* expression
536 restricts interneurons to AACs. Height of green or gray shade represents relative expression levels.

537 b) Configuration of triple allele intersectional labeling, combining *Unc5b-CreER* and *Nkx2.1-Flp*
538 drivers and the Cre-AND-Flp *Ai65* reporter. Embryonic Flp expression removes the frt-flanked
539 STOP cassette and postnatal *Cre*ER induction removes the loxp-flanked STOP, thereby activating
540 constitutive tdTomato expression.

541 c) Schematic showing that MGE-derived AACs migrate and populate all four pallial-derived brain
542 structures depicted in color: medial pallium (red), dorsal pallium (green), lateral pallium (violet and
543 blue), and ventral pallium (yellow and orange). Adapted from Puelles, 2017.

544 d) Representative midsagittal section showing AAC labeling in cerebral cortex, hippocampal
545 formation (HPF), and olfactory centers such as piriform cortex (PIR) and anterior olfactory nucleus
546 (AON). Note sparse labeling in lateral hypothalamus (LH) and striatum (str).

547 e-g) Representative coronal sections at specified anterior-posterior coordinates (from Bregma)
548 showing dense AAC labelling in cerebral cortex (e-g), HPF (f-g), claustrum (CLA, e), endopiriform
549 (EP, f,-g), taenia tecta (TTd, e), lateral septum (LS, e), basolateral amygdala (BLA, f-g), cortical
550 amygdala (COA, f-g), medial amygdala (MeA, f), and hypothalamus (HYP, g). (Scale bars, 500µm.)
551 Abbreviations for anatomical structures are listed in Appendix.

552

553 **Figure 1 Supplement Figure 1. Dense labelling of AACs across brain regions in a *Unc5b-***
554 ***CreER;Nkx2.1-Flp;Ai65* mouse.**

555 (a-f) Additional representative coronal sections showing dense Ai65 expression patterns at specified
556 anterior-posterior coordinates (from Bregma). Note labeling in cerebral cortex (a-f); hippocampus
557 (e-f); olfactory centers (PIR, AON, TTd) (a-b); AI, CLA, EP (b-c); COA, BLA, MeA (d-f); BST (d);
558 and HYP (e-f). (Scale bars, 500µm.)

559 (g-j) Ai65-labelled pAACs in the bed nuclei of the stria terminalis (BST) are largely confined to the
560 principal nucleus (BSTpr), with pAACs clustering more densely in anterior BSTpr (f-g) compared to
561 more posterior segments (h-i).

562 (k-n) Ai65-labelled pAACs in the hypothalamus are densest in the ventral-medially area of the
563 arcuate nucleus, with highest density in caudal portions (j-l), and more posteriorly in the
564 paraventricular hypothalamic nuclei (m). pAACs are also present sparsely in the dorsal-medial
565 nucleus of the hypothalamus (j-l).

566

Figure 1 Supplement Figure 2. Additional sagittal sections of *Unc5b-CreER; Nkx2.1-Flp; Ai65* mice highlighting dense pAACs in medial, lateral, and ventral pallium-derived structures.

(a-c) A lateral sagittal section showing the lPAL-derived anterior insular (AI), claustrum (CLA), endopiriform (EP) (magnified in b) and mPAL-derived hippocampal formation (magnified in c). Note the single-banded orientation of hippocampal (c) and insular (b) AACs that is absent in more inferior lPAL structures (b).

(d-e), A more medial sagittal section showing dorsal and ventral hippocampus and retrohippocampal region (RHP) (d), retrohippocampus, and visual and retrosplenial cortex (e). Compare the dual-banded AAC distribution in upper and deeper cortical layers to the single-banded pattern in hippocampus. Also note dense labeling in BLA, COA, and MeA (a, d). (Scale bars, 500µm.)

Figure 1 Supplement Figure 3. Intersectional targeting with *Pthlh-Flp* and *Nkx2.1-Cre* or *Nkx2.1-CreER* reveals similar AAC distribution compared to *Unc5b-CreER;Nkx2.1-Flp*.

(a) Schematic of intersectional strategy.

(b-d) Tamoxifen induction of *Nkx2.1-CreER; Pthlh-Flp; Ai65* at E14.5 or E17.5 sparsely labels ChCs with diverse morphology in sensorimotor cortices. Arrowheads highlight a translaminar AAC type in layer 2, which extends axon arbors into deep layers. (Scale bars, 65µm.).

(e-i) Coronal hemisections from *Nkx2.1-Cre; Pthlh-Flp; Ai65* at specified anterior-posterior coordinates (mm from Bregma) showing pattern of dense labeling. Note labeling in cerebral cortex (e-i); hippocampus (h-i); olfactory centers (PIR, AON, TTd) (e-h); AI, CLA, EP (f); COA, BLA, MeA (h-i); and HYP (i). Labeling by *Nkx2.1-Cre; Pthlh-Flp* is sparser in AON and anterior TTd and absent in BST compared to *Unc5b-CreER; Nkx2.1-Flp* (Fig1). Note non-AAC labeling of layer 4 interneurons in somatosensory cortex (g-h) and striatum (CP, f-h). The absence of projection fibers in SNr (i) suggests these striatal cells are not medium spiny neurons and likely striatal interneurons (Scale bars, 500µm.).

(j-l) Coronal hemisections from *Nkx2.1-CreER; Pthlh-Flp; Ai65* following a single tamoxifen dose at embryonic day 18.5 (E18.5) shows exclusive specificity for individual ChCs across neocortex (Scale bars, 500µm.)

(m) Intersectional strategy of *Pthlh* and *VIP* using *VIP-Cre;Pthlh-Flp; Ai65* mice.

(n-p) Dense labeling of cortical and hippocampal interneurons with predominantly bipolar morphology (putative interneuron-selective cells) in cortical layers II/III and deep layers (Scale bars, 500µm.)

Figure 2. Characterization of chandelier cells (ChCs, i.e. cortical AACs) in cerebral cortex.

(a) Representative 2D stereotactic plot of cortical ChC distribution in *Unc5b; Nkx2.1*. Dots represents individual RFP-labelled cells. Anterior-posterior distance from Bregma (vertical scale on right).

603 (b) Normalized ChC cell density (cells/um^3) following registration to ARAv3 isocortical areas. For b
604 and c, data are mean ± SEM.

605 (c) Comparative bar plot showing relative proportion in each cortical layer in sensorimotor cortices.

606 (d) Violin plots of ChC cell density proportion along pia-to-white matter cortical depth in each
607 sensorimotor cortical areas. Median is used for each violin plot.

608 (e) Scatterplot of ChC distribution along pia-to-white matter depth (vertical axis) and anterior-
609 posterior distance from Bregma (horizontal axis, in mm); red dots represent individual cells. While a
610 vast majority (~80%) of ChCs occupy a band near the layer I/II border, ChCs in other layers account
611 for ~20% of the total cortical population and vary in depth distribution by anterior-posterior cortical
612 location.

613 (f) Representative ChC laminar distribution pattern, showing largely separated supragranular (top
614 inset) and infragranular (bottom inset) laminar subtypes. (Scale bars, 200µm and insets, 100 µm.)

615 (g-i) Multiple ChC laminar subtypes revealed by single-cell labeling using low-dose tamoxifen
616 induction.

617 These include supragranular subtypes (g), intragranular and inverted subtypes (h), and translaminar
618 L2/3 subtypes that extend long vertical axons (white arrowheads) to deep layers (i). White
619 arrowheads highlight axonal plexi distant from soma in translaminar types. (Scale bars, 65µm.)

620 (j) Example of regional ChC morphological diversity in auditory cortex, with relatively high
621 proportion of translaminar subtypes. (Scale bar, 200µm.)

622 (k-n) ChC axon terminal (i.e. "cartridge") labeling and mapping using intersectional synaptophysin-
623 EGFP/cytoplasmic-tdtomato reporter mouse line.

624 (k) Diagram of intersectional genetic labeling of ChC cartridges (EGFP) and soma (tdTomato).

625 (l) Pixel classifier trained to segment EGFP-expressing ChC cartridges in cortex and CA1
626 hippocampus. White arrowheads indicate detected EGFP-labelled cartridges. (Scale bars, 100µm).

627 (m) Density of ChC catridges (catridges/um^3) registered to ARAv3

628 (n) Representative relative depth plots (from pia) of individual detected cartridges at a single AP
629 coordinate for each cortical area. Refer to Appendix for ARAv3 area label abbreviations. Note
630 reduced deep layer cartridges in V1 and FRP, RSP.

631 **Figure 2 Supplement Figure 1. Anatomical diversity of ChCs across neocortical areas.**

632 AnkyrinG or IκBα immunohistochemical labeling (green) of PyN AIS was used for validation of
633 axo-axonic targeting. Examples are shown of characteristic upper L2 ChCs in motor (a), sensory (b,
634 d,j), cingulate (f, k), and insular cortex (i). Examples of deeper L5 or L6 ChCs in somatosensory (c,
635 e, g) and temporal association area (TEA) (h). Note the clustering of a distinct morphological
636 subtypes in ventromedial infralimbic cortex (l). High-magnification inset (g): white arrowheads
637 indicate segments of overlap between AnkG and RFP. Scale bars, 50µm and 5µm for high-
638 magnification insets.

639 **Figure 3. Distribution and validation of AACs in hippocampus.**

640 (a) Population labeling of AACs throughout hippocampal compartments by *Unc5b; Nkx2.1*
641 intersection. Note the highly-stereotyped banded distribution of AACs in CA1-CA3, with somata in
642 the stratum pyramidale and vertically oriented dendrites extending basally to the stratum oriens and
643 apically to the striatum lacunosum-moleculare. AACs are much sparser in dentate gyrus, with
644 individual cells having elaborate and extended horizontal axon arbor. Scale bars, 200µm and 50µm
645 for high-magnification inset.

646 (b) AACs in ventral CA1 have overall similar morphology as in dorsal CA1, though with longer
647 basal-apical dendrites matching the ventral CA1 anatomy.

648 (c) Normalized AAC cell density (cells/um^3) across hippocampal compartments. CA2 has 3-4-fold
649 higher AAC cell density compared to CA1 and CA3 and 12-fold higher compared to DG.

650 (d-i) Immunohistochemistry validation with the AIS markers AnkG or IκBα (green) and sparse-
651 labelled RFP cells confirm axo-axonic targeting by the intersectional strategy. Examples of
652 hippocampal AACs in CA1 (e, g), CA2 (d) and CA3 (d, f, h). In contrast, AACs in DG have much
653 wider axon arbor in the stratum granulosum, potentially innervating many more granule cell AIS
654 compared to in other hippocampal compartments (i). High-magnification inset: white arrowheads
655 indicate segments of IκBα and RFP apposition. (Scale bars, 50µm and 20µm for high-magnification
656 inset.) For b, data are mean ± SEM.

657

658 **Figure 4. Distribution of AACs across lPAL- and vPAL-derived structures**

659 (a) Dense labelled RFP cells in claustrum, endopiriform nucleus, and insula. Note AACs in insula
660 follow the banded laminar pattern of AACs similar to cortical upper layers and piriform, while those
661 in claustrum and endopiriform are more dispersed in distribution.
662

663 (b-c) Sparse labeling of single cell morphologies in endopiriform nucleus (b) and claustrum (c)
664 showing elaborate dendritic and axonal branching structure.

665 (d) Normalized AAC cell density (cells/um^3) across lateral pallial structures. pAACs are
666 approximately five-fold more prevalent in dorsal EP compared to ventral EP. Data are mean ± SEM.

667 (e) Dense labelling throughout vPall-derived amygdalar nuclei and piriform cortex. Note there is a
668 degree of compartmentalization, with fewer cells in the ventral-most portions of EPd and the ventral
669 BMA. The laminar pattern of AAC distribution in piriform and Piriform-amygdalar area (PAA) is
670 similar to other three-layered allocortices.

671 (f-h) Immunohistochemistry of single cell labeling shows the multipolar morphologies characteristic
672 of amygadalar AACs. High-magnification inset: white arrowheads indicate segments of AnkG and
673 RFP apposition. (Scale bars, 500 µm for grayscale panels, 50µm and 5µm for single cell examples
674 and insets.)

675 (i-j) Normalized AAC cell density (cells/um^3) across cortical subplate (i) and striatum-like (j)
676 amygdala. Data are mean ± SEM.

677 **Figure 5. ACCs in piriform cortex.**

678 (a-c) Dense AAC labelling in piriform cortex, organized from anterior (a) to posterior (c) and
679 overlaid with ARAv3 area outlines. Note the highly laminar distribution patterns.

680 (d-j). Examples of single piriform AACs co-stained with AnkG (green). Note the relatively similar
681 morphologies with only a few apical dendrites extending to the pial surface (d-g, i-j). An example of
682 a deeper layer AAC at the border of piriform and EPv (h). White arrowheads in high-magnification
683 insets indicate segments of overlap for RFP-labelled AAC and AnkG-labelled AIS. (Scale bars,
684 500µm for grayscale images, 50µm for confocal, 10µm for high-magnification insets.)

685 **Figure 6. Identification and distribution of novel AAC subpopulations in anterior olfactory**
686 **nucleus (AON), taenia tecta (TT), and septum.**

687 (a-b) Dense population labeling in anterior AON and TT (a) and more posterior sections containing
688 the TT and LS (b). Anteriorly, AACs are more concentrated in ventral TT while posteriorly in dorsal
689 TT. Within LS, AACs tend to occupy the medial most portions along the midline.

690 (c-g, i-k) Single cell (confocal) labeling of AACs in anterior olfactory nucleus (c-d), taenia tecta (e-
691 g), and lateral septum (i-k). Note that despite areal variations, individual AACs preserve their
692 stereotyped morphological characteristics (apical-oriented dendrite and basal-oriented axon arbor)
693 that conform to laminar patterns of targets in each anatomical area. High-magnification insets: white
694 arrowheads indicate segments of AnkG and RFP apposition. (Scale bars, 200 µm for grayscale
695 panels, 50µm and 5µm for single cell examples and insets.)

696 (h) Normalized cell density (cells/um^3) for AACs in AON, TT, and lateral septum. Within lateral
697 septum, the majority of AACs are located in rostral compartments (LSr). Data are mean ± SEM.

698 **Figure 7. Intersectional tTA2 conversion enables viral access and input tracing to ChCs in**
699 **sensorimotor cortices.**

700 (a) Schematic of intersectional tTA2-conversion strategy. Expression of *Nkx2.1-Flp* and subsequent
701 *Unc5b-CreER* or *PV-Cre* results in activation of tTA2 expression in AACs. This provides a genetic
702 handle for versatile viral targeting and manipulation.

703 (b) Cortical injection of TRE3G-promoter AAV vectors enables specific targeting of ChCs (green,
704 left). A similar backbone was used to construct a TRE3G rabies starter AAV for monosynaptic input
705 tracing, which contains both TVA and optimized rabies glycoprotein (right). Compared to TRE3G-
706 EGFP, the TRE3G starter AAV has weaker EGFP labeling of neurites. (Scale bar, 200µm.)

707 (c) Linear regression fit of inputs cells/starter cells. Each point represents one animal, n= 18, r =
708 0.8874, slope = 135.51.

709 (d) Relative pia-to-white matter depth distribution of starter cells (expressing both AAV starter and
710 rabies). ChC starter cell tended to cluster closer to the pia while PV cells were more broadly
711 distributed throughout the cortical upper layers, reflecting the differences in the distribution of the
712 two subtypes.

713 (e-g) Synaptic input source to ChCs in MOs, MOp, and SSp, with PV cells as comparison.

714 Left: representative coronal sections from three indicated cortical areas overlaid with macroscale
715 view of rabies tract labeling (in red, gray is autofluorescence) to each subpopulation of ChC.

716 Middle: Histogram comparing percentage of inputs from each structure innervating the indicated
717 cortical subpopulation of ChCs (dark gray) and PV (light gray), sorted from largest input source to
718 smallest. Inset: Representative top-down map of all inputs to AACs from a single animal.

719 Right: Representative sections highlighting select sources of rabies-labelled inputs to each ChC
720 population, overlaid with ARAv3 boundaries. (Scale bars, 200µm.) For e-g, data are mean ± SEM,
721 **P < 0.01, ***P < 0.001, ****P < 0.0001 indicates P ≥ 0.05 (two-way ANOVA with post hoc
722 Bonferroni correction); for scatterplot in d, median is plotted. Homotypic projections to injection site
723 from contralateral hemisphere are denoted by (#)

724 For each MOs, MOp and SSp, N=6 mice for (3 *Unc5b; Nkx2.1*, 3 *PV; Nkx2.1*; total N=18 mice)

725 **Figure 7 Supplement Figure 1. Intersectional tTA2 conversion enables viral access and input**
726 **tracing to ChCs and PV cells**.

727 (a) Schematic and procedure for synaptic input tracing from ChC and PV interneurons. Top, driver
728 and reporter lines to achieve tTA expression in ChC or PV cells. Middle, schematic of AAV and
729 EnvA pseudo-typed rabies viral vectors. Bottom, timeline of tamoxifen and viral vector for
730 retrograde synaptic tracing.

731 (b) Bulk injection of TRE3G-EGFP in *Unc5b-CreER; Nkx2.1-Flp; LSL-FSF-tTA2* results in
732 efficient and specific labeling of ChCs, identifiable by laminar position and morphological features
733 (inset). (Scale bars, 200µm and 100µm for high-magnification inset.)

734 (c) Starter AAV expression is comparable to TRE3G-EGFP with high specificity for ChCs in *Unc5b;*
735 *Nkx2.1*, albeit with weaker EGFP neurite expression. (Scale bars, 100µm and 20µm for high-
736 magnification insets.)

737 (d, e) Example of starter cells (arrowheads) co-expressing EGFP (AAV vector) and RFP (rabies
738 vector) in *Unc5b/Nkx2.1* (d) and *PV/Nkx2.1* (e) intersections. (Scale bars, 100µm and 20µm for
739 high-magnification insets.)

740 **Figure 8. Monosynaptic input tracing to AACs^{CA1} of hippocampus**.

741 (a) Schematic of retrograde synaptic tracing from CA1 AACs with site of viral injection.

742 (b) Starter AAV expression in CA1 (green). White arrowheads show soma position is largely
743 confined to the pyramidal cell layer. (Scale bar, 50µm.)

744 (c) Comparative input distribution from ipsilateral (right) and contralateral (left) hippocampal
745 compartments.

746 (d) Mesoscale rabies labeling of presynaptic input cells (red) to AACs^{CA1}

747 (e) Histogram of percentage of total inputs from each structure, sorted from largest to smallest. Inset:
748 Summary schematic of input sources to AACs^{CA1}. AACs^{CA1}receive strong innervation from

749 entorhinal, subiculum, and contralateral hippocampus, with more minor innervation from thalamus,
750 medial septum, diagonal band nucleus, and various cortical areas.

751 (f-j) Immunohistochemistry and HCR RNA-FISH marker analysis of input cells in medial septum
752 (MS) and nucleus of the diagonal band (NDB), indicated by color-coded labels. Examples of co-
753 labeled cells are shown following HCR RNA-FISH for the inhibitory marker vGAT (g) and
754 immunohistochemistry for the excitatory marker EAAC1 (h), PV (i) and ChAT (j). White
755 arrowheads indicate co-labelled cells for each marker. (Scale bars, 50µm and 20µm for high-
756 magnification insets.)

757 (k) Quantification of marker colocalization with rabies labeling in MS and NDB.

758 (l-p) Representative coronal sections highlighting select sources of rabies-labelled inputs to
759 $AACs^{CA1}$, overlaid with ARAv3 atlas boundaries. Inputs within hippocampus were mostly from
760 within CA1 both ipsilateral (l) and contralateral (m) to the injection site. Input cells were also found
761 in adjacent cortical areas more posterior such as entorhinal cortex (ENT), auditory cortex (AUD),
762 and temporal association area (TEa) (n-p). Thalamic inputs were largely confined to the anterior
763 group of the dorsal thalamus (ATN) (o). (Scale bars, 200µm.)

764 For c, e, and k, data are mean ± SEM from N=4 mice. Homotypic projections to injection site from
765 contralateral hemisphere are denoted by (#CA1) in e.

766 **Figure 9. Monosynaptic input tracing to $AACs^{BLA}$.**

767 (a) Schematic of retrograde synaptic tracing from BLA AACs with site of viral injection.

768 (b) Starter AAV distribution as indicated by white arrowheads, overlaid with ARAv3 atlas. (Scale
769 bar, 200µm.)

770 (c) Left: Mesoscale rabies labeling of presynaptic input cells (red) to $AACs^{BLA}$. Right: Histogram of
771 percentage of total inputs from each structure, sorted form largest to smallest. Inset: Summary
772 schematic synaptic input source to $AACs^{BLA}$. $AACs^{BLA}$ are innervated by diverse sets of inputs, with
773 strongest innervation from entorhinal cortical-hippocampal network (EC-HPC), piriform areas (PIR),
774 cortical subplate (CTXsp), and minor subcortical and cortical inputs

775 (d-j) Representative coronal sections of rabies-labelled inputs (grey) across input structures, overlaid
776 with ARAv3 boundaries. (Scale bars, 200µm.) Inputs to $AACs^{BLA}$ were found in amygdalar and
777 cortical-amygdalar areas (d-e), piriform (e), midline group of the dorsal thalamus (f), substantia
778 innominata (g), posterior hippocampus and cortex (h) and the ventral subiculum (i). Examples of
779 dense input cells in medial (MEZ) and lateral (LZ) hypothalamus overlaid with excitatory vGLUT2
780 HCR RNA-FISH (j).

781 (k-o) Immunohistochemistry and RNA-FISH marker analysis of input cells in striatum/CP, GPe, EP,
782 and hypothalamus. VGAT FISH or GABA IHC were used for identifying GABAergic input cells (l-
783 n) while VGLUT2 FISH was used an excitatory marker (o) as indicated. White arrowheads indicate
784 co-labelled cells. (Scale bars, 50µm and 20µm for high-magnification insets.) Right: Quantification
785 of marker colocalization with rabies labeling for each corresponding area. Inputs to $AACs^{BLA}$ from

786 CP, GPe, and EP were inhibitory, while inputs from hypothalamus were excitatory. Data are mean ±
787 SEM from N=3 mice.

788

789 **Materials and Methods**

790 **Key Resources Tables**

Reagent type (species) or resource	Designation	Source or reference	Identifiers	Additional information
Antibody	Anti-AnkryinG (mouse monoclonal)	Neuromab	Cat#: 75-146	1:500
Antibody	Anti-ChAT (goat polyclonal)	Millipore	Cat#: AB144P	1:300
Antibody	Anti-EAAC1 (goat polyclonal)	Millipore	Cat#: AB1520	1:500
Antibody	Anti-GABA (rabbit polyclonal)	Sigma	Cat#: A2052	1:500
Antibody	Anti-GFP (chicken polyclonal)	Aves Labs	Cat#: 1020	1:1000
Antibody	Anti-parvalbumin (mouse monoclonal)	Sigma	Cat#: P3088	1:1000
Antibody	Anti-Phospho-IκBα (rabbit polyclonal)	Cell Signaling Technology	Cat#: 2859	1:500
Antibody	Anti-RFP (rabbit polyclonal)	Rockland	Cat#: 600-401-379	1:1000
Commercial assay or kit	HCR v3.0	Molecular Instruments		
Other	AAVDJ-TRE3g-EGFP	Vigene		Adeno-associated virus, titer: 5 × 1012 genome copies (gc)/ml
Other	AAVDJ-TRE3g-TVA-oG-EGFP	Vigene		Adeno-associated virus, titer: 9.24 × 1012 genome copies (gc)/ml
Other	G-Deleted Rabies dsRedXpress	Salk Institute		Rabies virus, titer: 5.0 × 10^7 colony-forming units (cfu)/ml
Software, algorithm	ImageJ	NIH	RRID:SCR_003070	
Software, algorithm	MATLAB	Mathworks	R2017b RRID:SCR_001622	
Strain (Mus musculus)	Ai65	The Jackson Laboratory	021875 RRID:IMSR_JAX:021875	
Strain (Mus musculus)	C57BL/6J	The Jackson Laboratory	000664 RRID:IMSR_JAX:000664	

Strain (Mus musculus)	dual-SynaptotagminEGFP-2A-tdTomato	The Jackson Laboratory	030206 RRID:IMSR_JAX:030206	
Strain (Mus musculus)	dual-tTA2	The Jackson Laboratory	036304 RRID:IMSR_JAX:036304	
Strain (Mus musculus)	Nkx2.1-Cre	The Jackson Laboratory	008661 RRID:IMSR_JAX:008661	
Strain (Mus musculus)	Nkx2.1-FlpO	The Jackson Laboratory	028577 RRID:IMSR_JAX:028577	
Strain (Mus musculus)	Pthlh-FlpO			
Strain (Mus musculus)	PV-Cre	The Jackson Laboratory	017320 RRID:IMSR_JAX:017320	
Strain (Mus musculus)	Unc5b-CreER			

791

792 **Animals**

793 All experiments were carried out in accordance with the guidelines of the Animal Care and Use
794 Committee of Cold Spring Harbor Laboratory (CSHL). Mice were housed in groups of five per cage
795 or singly if pregnant under standard vivarium conditions with a 12 h light/dark cycle. Unc5b-CreER
796 (Dudok et al., 2021) or PV-Cre (JAX, Stock 017320) were crossed to Nkx2.1-Flp (JAX, Stock
797 028577). Pthlh-Flp (unpublished) was crossed to Nkx2.1-Cre (JAX, Stock 008661). For each
798 Cre/Flp combination, offspring hemizygous for both alleles were crossed to Ai65 (JAX, Stock
799 021875), Rosa26-loxpSTOPloxp-frtSTOPfrt-synaptotagminEGFP-2A-tdTomato (JAX, Stock
800 030206), or Rosa26-loxpSTOPloxp-frtSTOPfrt-tTA2 (JAX, Stock 036304) reporter mice. Mice with
801 Unc5b-CreER were induced by tamoxifen i.p. (TM; Sigma-Aldrich, Cat# T5648) administered either
802 1) for dense labelling and input tracing, 100mg/kg for five consecutive days starting at P55-60 2) for
803 single cell labeling, 25mg/kg for 1-2 consecutive days at P55-P60. Animals were fed ad libitum and
804 their health status were routinely monitored. Both male and female animals were used in all
805 experiments, with 3-4 mice total for each injection site x genotype and for cell distribution analysis.
806 Genotyping was performed using PCR and according to supplier protocols.
807

808 **Immunohistochemistry**

809 Mice were anesthetized with Avertin and transcardially perfused with 0.9% saline followed by 4%
810 paraformaldehyde in 0.1M phosphate buffer. Following overnight post-fixation, brains were rinsed
811 in PBS and sectioned at 50-65µm thickness with a Leica VT1000S vibratome. For
812 immunohistochemistry, sections were first treated with a secondary-matched blocking solution (10%
813 normal goat or donkey serum and 0.2% Triton-X100 in PBS) for 1 hr, then incubated overnight at
814 4°C with primary antibodies diluted in 5% blocking solution. Sections were washed three times in
815 PBS and incubated for 2h at room temperature with corresponding secondary antibodies, Goat or
816 Donkey Alexa Fluor 488, 568 or 647 (1:500, Life Technologies) and DAPI to label nuclei (1:1000 in
817 PBS, Life Technologies, Cat# 33342). Sections were washed three times with PBS and dry-mounted

818 on slides using Fluoromount-G (SouthernBiotech, Cat# 0100-01) mounting medium. Primary
819 antibodies used were Anti-AnkryinG (1:500, Neuromab, Cat#: 75-146), Anti-ChAT (1:300,
820 Millipore, Cat#: AB144P), Anti-EAAC1 (1:500, Millipore, Cat#: AB1520), Anti-GABA (1:500,
821 Sigma-Aldrich, Cat#: A2052), Anti-GFP (1:1000, Aves Labs, Cat#: 1020), Anti-parvalbumin
822 (1:1000, Sigma-Aldrich, Cat#: P3088), Anti-Phospho-IκBα (1:500, Cell Signaling Technology, Cat#:
823 2859), Anti-RFP (1:1000, Rockland, Cat#: 600-401-379). Samples for AAC validation were
824 collected from 6 mice given 25mg/kg for 1-2 consecutive days, as described above.
825
826 **Floating section two-color in situ hybridization**
827 In situ hybridization was performed using hybridization chain reaction (HCR v3.0, Molecular
828 Instruments). Samples post-fixed in 4% PFA at 4°C were cryoprotected in 30% sucrose solution in
829 RNAse-free PBS (DEPC-PBS) at 4°C for 48 hr, frozen in Tissue-Tek O.C.T. Compound (Sakura),
830 and stored at –80°C until sectioning. 50 µm thick coronal floating sections were collected into a
831 sterile 24-well plate in DEPC-PBS, fixed again briefly for 5 min in 4% PFA, then placed in 70%
832 EtOH in DEPC-PBS overnight. Sections were rinsed in DEPC-PBS, incubated for 45 min in 5%
833 SDS in DEPC-PBS, rinsed and incubated in 2x SSCT, pre-incubated in HCR hybridization buffer at
834 37°C, and then placed in HCR hybridization buffer containing RNA probes overnight at 37°C. The
835 next day, sections were rinsed 4 × 15 min at 37°C in HCR probe wash buffer, rinsed with 2X SSCT,
836 pre-incubated with HCR amplification buffer, then incubated in HCR amplification buffer
837 containing HCR amplifiers at room temperature for ~24 hr. On the final day, sections were rinsed in
838 2x SSCT, rinsed again with 2x SSCT, then mounted on slides and coverslipped with Fluoromount-G
839 (Southern Biotech).
840
841 **Microcopy and image analysis**
842 Confocal imaging was performed on a Zeiss LSM 780 (CSHL St. Giles Advanced Microscopy
843 Center) using 10x, 20x, or 63x objectives. Imaging for grayscale overview images was performed on
844 a Zeiss Axioimager M2 System equipped with MBF Neurolucida Software (MBF) using 5x, 10x, or
845 20x objectives. Quantification and image analysis was performed using Image J/FIJI software.
846 Statistics and plotting of graphs were done using GraphPad Prism 7 and Microsoft Excel 2010.
847
848 **Viruses**
849 To construct AAVDJ-TRE3g-TVA-oG-eGFP, TVA, the optimized rabies glycoprotein oG (Kim et
850 al., 2016), and eGFP were linked by 'self-cleaving' 2A and P2A peptides and cloned into pAAV-
851 TRE3G (Sacha Nelson). For AAVDJ-TRE3g-eGFP only eGFP was cloned. AAVs serotype DJ were
852 packaged by a commercial vector core facility (Vigene). Genomic titers of AAVDJ-TRE3g-TVA-
853 oG-eGFP and AAVDJ-TRE3g-eGFP were 9.24×10^{12} gc/ml and 5.0×10^{12} gc/ml, respectively.
854 TVA, oG, and eGFP were subcloned from AAV-hSyn-FLEX-TVA-P2A-EGFP-2A-oG (Addgene,
855 Cat# 85225). AAVs were diluted 1:5 in 1x PBS immediately prior to use. EnvA-pseudotyped G-
856 Deleted Rabies dsRedXpress was purchased from Salk Institute (5.0 × 10^7 titer units (TU)/ml).
857
858 **Stereotactic viral injections**
859 Adult mice were anaesthetized with 2% isofluorane delivered by constant air flow (0.4 L/min).
860 Analgesics ketoprofen (5 mg/kg) and dexamethasone (0.5 mg/kg) were administered subcutaneously
861 just prior to sugery, while lidocaine (2-4 mg/kg) was applied intra-inciscionally. Mice were mounted
862 on a stereotaxic headframe (Kopf Instruments, 940 series or Leica Biosystems, Angle Two) and
863 stereotactic coordinates identified as follows, (MOs): 2.25mm anterior to bregma, 1.2mm lateral,
864 0.3mm in depth; (MOp): 0.5mm anterior to bregma, 1.6mm lateral, 0.3mm in depth; (SSp): 1.12mm
865 posterior to bregma, 3.25mm lateral, 0.3mm in depth; (CA1): 1.94mm posterior to bregma, 1.4mm
866 lateral, 1.4mm in depth ; (BLA): 1.9mm posterior to bregma, 3.38mm lateral, 4.76mm in depth. An

incision was made over the scalp, a small burr hole drilled in the skull and brain surface exposed. A pulled glass pipette with a tip of 20–30 µm containing virus was lowered into the brain. Virus was delivered at a rate of 30nL/min using a Picospritzer (General Valve Corp) for a total volume of 100-150nL for starter AAV and 300-400nL for rabies virus. The pipette remained in place for 10 min prior to retraction to prevent backflow, after which the incision was closed with 5/0 nylon suture thread (Ethilon Nylon Suture Ethicon) or Tissueglue (3M Vetbond). Mice were kept warm on a heating pad until complete recovery. For input tracing experiments, *Unc5b-CreER; Nkx2.1-Flp; dual-tTA2* (tamoxifen-induced as described above) and *PV-Cre; Nkx2.1-Flp; dual-tTA2* were injected at respective coordinates with AAVDJ-TRE3g-TVA-oG-eGFP at P75±2. After a 2-3 week incubation period, a second injection at the same coordinates was performed using EnvA-pseudotyped G-Deleted Rabies-dsRedXpress. Following another 7 day incubation mice were perfused as described above.

Whole-brain STP tomography and image analysis

We used the whole-brain STP tomography pipeline described previously (Ragan et al., 2012; Kim et al., 2017; Matho et al., 2021). Perfused and post-fixed brains were embedded in 4% oxidized-agarose in 0.05 M PB, cross-linked in 0.2% sodium borohydrate solution (in 0.05 M sodium borate buffer, pH 9.0–9.5). The entire brain was imaged coronally with a 20× Olympus XLUMPLFLN20XW lens (NA 1.0) on a TissueCyte 1000 (Tissuevision) with a Chameleon Ultrafast-2 Ti:Sapphire laser (Coherent). EGFP/EYFP or tdTomato/dsRedXpress signals were excited at 910 nm or 920 nm, respectively. Whole-brain image sets were acquired as series of 12 (x) × 16 (y) tiles with 1 µm × 1 µm sampling for 230–270 z sections with a 50-µm z-step size. Images were collected by two PMTs (PMT, Hamamatsu, R3896), for signal and autofluorescent background, using a 560-nm dichroic mirror (Chroma, T560LPXR) and band-pass filters (Semrock FF01-680/SP-25). The image tiles were corrected to remove illumination artifacts along the edges and stitched as a grid sequence. Image processing was completed using ImageJ/FIJI and Adobe/Photoshop software with linear level and nonlinear curve adjustments applied only to entire images. Registration of brain-wide datasets to the Allen reference Common Coordinate Framework version 3 (CCFv3) was performed by 3D affine registration followed by a 3D B-spline registration using Elastix software (Klein et al., 2010), according to established parameters. Somata labelled by Ai65-tdtomato or rabies-dsRedXpress and catridges labelled by synaptotagmin-EGFP were automatically detected by a convolutional network trained as described previously (Ragan et al., 2012; Kim et al., 2017; Matho et al., 2021). For AAC laminar depth, somata and cartridge coordinates were overlaid on a mask for relative cortical depth, as described. For area cell density and cortical depth analysis, we registered each dataset, reporting cells detected in each brain structure without warping the imaging channel. All cell density quantifications are reported as mean cells per cubic µm ± SEM from n=4 mice.

Data availability

The data that support the findings of this study are presented in Source data 1.

References

Bakken, T. E., Jorstad, N. L., Hu, Q., Lake, B. B., Tian, W., Kalmbach, B. E., Crow, M., Hodge, R. D., Krienen, F. M., Sorensen, S. A., Eggermont, J., Yao, Z., Aevermann, B. D., Aldridge, A. I., Bartlett, A., Bertagnolli, D., Casper, T., Castanon, R. G., Crichton, K., . . . Lein, E. S. (2021). Comparative cellular analysis of motor cortex in human, marmoset and mouse. *Nature*, *598*(7879), 111-119. https://doi.org/10.1038/s41586-021-03465-8

Bakken, T. E., Jorstad, N. L., Hu, Q., Lake, B. B., Tian, W., Kalmbach, B. E., Crow, M., Hodge, R. D., Krienen, F. M., Sorensen, S. A., Eggermont, J., Yao, Z., Aevermann, B. D., Aldridge, A. I., Bartlett, A., Bertagnolli, D., Casper, T., Castanon, R. G., Crichton, K., . . . Lein, E. S. (2021). Comparative cellular analysis of motor cortex in human, marmoset and mouse. *Nature*, *598*(7879), 111-119. https://doi.org/10.1038/s41586-021-03465-8

Beyeler, A., & Dabrowska, J. (2020). Neuronal diversity of the amygdala and the bed nucleus of the stria terminalis. *Handb Behav Neurosci*, *26*, 63-100. https://doi.org/10.1016/b978-0-12-815134-1.00003-9

Bienvenu, T. C., Busti, D., Magill, P. J., Ferraguti, F., & Capogna, M. (2012). Cell-type-specific recruitment of amygdala interneurons to hippocampal theta rhythm and noxious stimuli in vivo. *Neuron*, *74*(6), 1059-1074. https://doi.org/10.1016/j.neuron.2012.04.022

Daigle, T. L., Madisen, L., Hage, T. A., Valley, M. T., Knoblich, U., Larsen, R. S., Takeno, M. M., Huang, L., Gu, H., Larsen, R., Mills, M., Bosma-Moody, A., Siverts, L. A., Walker, M., Graybuck, L. T., Yao, Z., Fong, O., Nguyen, T. N., Garren, E., . . . Zeng, H. (2018). A Suite of Transgenic Driver and Reporter Mouse Lines with Enhanced Brain-Cell-Type Targeting and Functionality. *Cell*, *174*(2), 465-480.e422. https://doi.org/10.1016/j.cell.2018.06.035

DeFelipe, J., Hendry, S. H., Jones, E. G., & Schmechel, D. (1985). Variability in the terminations of GABAergic chandelier cell axons on initial segments of pyramidal cell axons in the monkey sensory-motor cortex. *J Comp Neurol*, *231*(3), 364-384. https://doi.org/10.1002/cne.902310307

Dudok, B., Szoboszlay, M., Paul, A., Klein, P. M., Liao, Z., Hwaun, E., Szabo, G. G., Geiller, T., Vancura, B., Wang, B.-S., McKenzie, S., Homidan, J., Klaver, L. M. F., English, D. F., Huang, Z. J., Buzsáki, G., Losonczy, A., & Soltesz, I. (2021). Recruitment and inhibitory action of hippocampal axo-axonic cells during behavior. *Neuron*, *109*(23), 3838-3850.e3838. https://doi.org/10.1016/j.neuron.2021.09.033

Fenno, L. E., Ramakrishnan, C., Kim, Y. S., Evans, K. E., Lo, M., Vesuna, S., Inoue, M., Cheung, K. Y. M., Yuen, E., Pichamoorthy, N., Hong, A. S. O., & Deisseroth, K. (2020). Comprehensive Dual- and Triple-Feature Intersectional Single-Vector Delivery of Diverse Functional Payloads to Cells of Behaving Mammals. *Neuron*, *107*(5), 836-853 e811. https://doi.org/10.1016/j.neuron.2020.06.003

Fish, K. N., Hoftman, G. D., Sheikh, W., Kitchens, M., & Lewis, D. A. (2013). Parvalbumin-containing chandelier and basket cell boutons have distinctive modes of maturation in monkey prefrontal cortex. *J Neurosci*, *33*(19), 8352-8358. https://doi.org/10.1523/JNEUROSCI.0306-13.2013

Fishell, G., & Kepecs, A. (2020). Interneuron Types as Attractors and Controllers. *Annual Review of Neuroscience*, *43*(1), 1-30. https://doi.org/10.1146/annurev-neuro-070918-050421

Fitzgerald, T. H., Valentin, A., Selway, R., & Richardson, M. P. (2013). Cross-frequency coupling within and between the human thalamus and neocortex. *Front Hum Neurosci*, *7*, 84. https://doi.org/10.3389/fnhum.2013.00084

Garcia-Moreno, F., Pedraza, M., Di Giovannantonio, L. G., Di Salvio, M., Lopez-Mascaraque, L., Simeone, A., & De Carlos, J. A. (2010). A neuronal migratory pathway crossing from diencephalon to telencephalon populates amygdala nuclei. *Nature Neuroscience*, *13*(6), 680-689. https://doi.org/10.1038/nn.2556

Gelman, D., Griveau, A., Dehorter, N., Teissier, A., Varela, C., Pla, R., Pierani, A., & Marin, O. (2011). A wide diversity of cortical GABAergic interneurons derives from the embryonic preoptic area. *J Neurosci*, *31*(46), 16570-16580. https://doi.org/10.1523/JNEUROSCI.4068-11.2011

Gouwens, N. W., Sorensen, S. A., Baftizadeh, F., Budzillo, A., Lee, B. R., Jarsky, T., Alfiler, L., Baker, K., Barkan, E., Berry, K., Bertagnolli, D., Bickley, K., Bomben, J., Braun, T., Brouner, K., Casper, T., Crichton, K.,

Daigle, T. L., Dalley, R., . . . Zeng, H. (2020). Integrated Morphoelectric and Transcriptomic Classification of Cortical GABAergic Cells. *Cell*, *183*(4), 935-953 e919. https://doi.org/10.1016/j.cell.2020.09.057

Hain, D., Gallego-Flores, T., Klinkmann, M., Macias, A., Ciirdaeva, E., Arends, A., Thum, C., Tushev, G., Kretschmer, F., Tosches, M. A., & Laurent, G. (2022). Molecular diversity and evolution of neuron types in the amniote brain. *Science*, *377*(6610), eabp8202. https://doi.org/10.1126/science.abp8202

Howard, A., Tamas, G., & Soltesz, I. (2005). Lighting the chandelier: new vistas for axo-axonic cells. *Trends Neurosci*, *28*(6), 310-316. https://doi.org/10.1016/j.tins.2005.04.004

Huang, Z. J., & Paul, A. (2019). The diversity of GABAergic neurons and neural communication elements. *Nature Reviews Neuroscience*, *20*(9), 563-572. https://doi.org/10.1038/s41583-019-0195-4

Ishino, Y., Yetman, M. J., Sossi, S. M., Steinecke, A., Hayano, Y., & Taniguchi, H. (2017). Regional Cellular Environment Shapes Phenotypic Variations of Hippocampal and Neocortical Chandelier Cells. *The Journal of Neuroscience*, *37*(41), 9901-9916. https://doi.org/10.1523/jneurosci.0047-17.2017

Kelly, S. M., Raudales, R., Moissidis, M., Kim, G., & Huang, Z. J. (2019). *Multipotent radial glia progenitors and fate-restricted intermediate progenitors sequentially generate diverse cortical interneuron types* [preprint]. http://biorxiv.org/lookup/doi/10.1101/735019

Klausberger, T., Magill, P. J., Márton, L. F., Roberts, J. D. B., Cobden, P. M., Buzsáki, G., & Somogyi, P. (2003). Brain-state- and cell-type-specific firing of hippocampal interneurons in vivo. *Nature*, *421*(6925), 844-848. https://doi.org/10.1038/nature01374

Lu, J., Tucciarone, J., Padilla-Coreano, N., He, M., Gordon, J. A., & Huang, Z. J. (2017). Selective inhibitory control of pyramidal neuron ensembles and cortical subnetworks by chandelier cells. *Nature Neuroscience*, *20*(10), 1377-1383. https://doi.org/10.1038/nn.4624

Magno, L., Asgarian, Z., Apanaviciute, M., Milner, Y., Bengoa-Vergniory, N., Rubin, A. N., & Kessaris, N. (2022). Fate mapping reveals mixed embryonic origin and unique developmental codes of mouse forebrain septal neurons. *Commun Biol*, *5*(1), 1137. https://doi.org/10.1038/s42003-022-04066-5

Miyoshi, G., Young, A., Petros, T., Karayannis, T., McKenzie Chang, M., Lavado, A., Iwano, T., Nakajima, M., Taniguchi, H., Huang, Z. J., Heintz, N., Oliver, G., Matsuzaki, F., Machold, R. P., & Fishell, G. (2015). Prox1 Regulates the Subtype-Specific Development of Caudal Ganglionic Eminence-Derived GABAergic Cortical Interneurons. *J Neurosci*, *35*(37), 12869-12889. https://doi.org/10.1523/JNEUROSCI.1164-15.2015

Munoz-Manchado, A. B., Bengtsson Gonzales, C., Zeisel, A., Munguba, H., Bekkouche, B., Skene, N. G., Lonnerberg, P., Ryge, J., Harris, K. D., Linnarsson, S., & Hjerling-Leffler, J. (2018). Diversity of Interneurons in the Dorsal Striatum Revealed by Single-Cell RNA Sequencing and PatchSeq. *Cell Rep*, *24*(8), 2179-2190 e2177. https://doi.org/10.1016/j.celrep.2018.07.053

Nakashima, M., Ikegaya, Y., & Morikawa, S. (2022). Genetic labeling of axo-axonic cells in the basolateral amygdala. *Neuroscience Research*, *178*, 33-40. https://doi.org/10.1016/j.neures.2022.02.002

Paul, A., Crow, M., Raudales, R., He, M., Gillis, J., & Huang, Z. J. (2017). Transcriptional Architecture of Synaptic Communication Delineates GABAergic Neuron Identity. *Cell*, *171*(3), 522-539.e520. https://doi.org/10.1016/j.cell.2017.08.032

Puelles, L. (2017). Comments on the Updated Tetrapartite Pallium Model in the Mouse and Chick, Featuring a Homologous Claustro-Insular Complex. *Brain Behav Evol*, *90*(2), 171-189. https://doi.org/10.1159/000479782

Qian, Y., Li, J., Zhao, S., Matthews, E. A., Adoff, M., Zhong, W., An, X., Yeo, M., Park, C., Yang, X., Wang, B. S., Southwell, D. G., & Huang, Z. J. (2022). Programmable RNA sensing for cell monitoring and manipulation. *Nature*, *610*(7933), 713-721. https://doi.org/10.1038/s41586-022-05280-1

Roux, L., & Buzsáki, G. (2015). Tasks for inhibitory interneurons in intact brain circuits. *Neuropharmacology*, *88*, 10-23. https://doi.org/10.1016/j.neuropharm.2014.09.011

Schneider-Mizell, C. M., Bodor, A. L., Collman, F., Brittain, D., Bleckert, A., Dorkenwald, S., Turner, N. L., Macrina, T., Lee, K., Lu, R., Wu, J., Zhuang, J., Nandi, A., Hu, B., Buchanan, J., Takeno, M. M., Torres, R., Mahalingam, G., Bumbarger, D. J., . . . Costa, N. M. D. (2021). Structure and function of axo-axonic inhibition. *eLife*, *10*. https://doi.org/10.7554/eLife.73783

1017 Somogyi, P. (1977). A specific 'axo-axonal' interneuron in the visual cortex of the rat. *Brain Research*, *136*(2),
1018 345-350. https://doi.org/10.1016/0006-8993(77)90808-3
1019 Somogyi, P., Freund, T. F., & Cowey, A. (1982). The axo-axonic interneuron in the cerebral cortex of the rat,
1020 cat and monkey. *Neuroscience*, *7*(11), 2577-2607. https://doi.org/10.1016/0306-4522(82)90086-0
1021 Szentágothai, J. (1975). The 'module-concept' in cerebral cortex architecture. *Brain Research*, *95*(2-3), 475-
1022 496. https://doi.org/10.1016/0006-8993(75)90122-5
1023 Tai, Y., Gallo, N. B., Wang, M., Yu, J.-R., & Van Aelst, L. (2019). Axo-axonic Innervation of Neocortical
1024 Pyramidal Neurons by GABAergic Chandelier Cells Requires AnkyrinG-Associated L1CAM. *Neuron*,
1025 *102*(2), 358-372.e359. https://doi.org/10.1016/j.neuron.2019.02.009
1026 Taniguchi, H., Lu, J., & Huang, Z. J. (2013). The Spatial and Temporal Origin of Chandelier Cells in Mouse
1027 Neocortex. *Science*, *339*(6115), 70-74. https://doi.org/10.1126/science.1227622
1028 Tasic, B., Yao, Z., Graybuck, L. T., Smith, K. A., Nguyen, T. N., Bertagnolli, D., Goldy, J., Garren, E., Economo,
1029 M. N., Viswanathan, S., Penn, O., Bakken, T., Menon, V., Miller, J., Fong, O., Hirokawa, K. E., Lathia,
1030 K., Rimorin, C., Tieu, M., . . . Zeng, H. (2018). Shared and distinct transcriptomic cell types across
1031 neocortical areas. *Nature*, *563*(7729), 72-78. https://doi.org/10.1038/s41586-018-0654-5
1032 Tosches, M. A. (2021). From Cell Types to an Integrated Understanding of Brain Evolution: The Case of the
1033 Cerebral Cortex. *Annu Rev Cell Dev Biol*, *37*, 495-517. https://doi.org/10.1146/annurev-cellbio-
1034 120319-112654
1035 Tremblay, R., Lee, S., & Rudy, B. (2016). GABAergic Interneurons in the Neocortex: From Cellular Properties
1036 to Circuits. *Neuron*, *91*(2), 260-292. https://doi.org/10.1016/j.neuron.2016.06.033
1037 Veres, J. M., Nagy, G. A., Vereczki, V. K., Andrási, T., & Hájos, N. (2014). Strategically Positioned Inhibitory
1038 Synapses of Axo-axonic Cells Potently Control Principal Neuron Spiking in the Basolateral Amygdala.
1039 *The Journal of Neuroscience*, *34*(49), 16194-16206. https://doi.org/10.1523/jneurosci.2232-14.2014
1040 Viney, T. J., Lasztoczi, B., Katona, L., Crump, M. G., Tukker, J. J., Klausberger, T., & Somogyi, P. (2013).
1041 Network state-dependent inhibition of identified hippocampal CA3 axo-axonic cells in vivo. *Nature*
1042 *Neuroscience*, *16*(12), 1802-1811. https://doi.org/10.1038/nn.3550
1043 Wang, B.-S., Bernardez Sarria, M. S., An, X., He, M., Alam, N. M., Prusky, G. T., Crair, M. C., & Huang, Z. J.
1044 (2021). Retinal and Callosal Activity-Dependent Chandelier Cell Elimination Shapes Binocularity in
1045 Primary Visual Cortex. *Neuron*, *109*(3), 502-515.e507. https://doi.org/10.1016/j.neuron.2020.11.004
1046 Wang, X., Tucciarone, J., Jiang, S., Yin, F., Wang, B.-S., Wang, D., Jia, Y., Jia, X., Li, Y., Yang, T., Xu, Z., Akram, M.
1047 A., Wang, Y., Zeng, S., Ascoli, G. A., Mitra, P., Gong, H., Luo, Q., & Huang, Z. J. (2019). Genetic Single
1048 Neuron Anatomy Reveals Fine Granularity of Cortical Axo-Axonic Cells. *Cell Reports*, *26*(11), 3145-
1049 3159.e3145. https://doi.org/10.1016/j.celrep.2019.02.040
1050 Zeppilli, S., Gurrola, A. O., Demetci, P., Brann, D. H., Attey, R., Zilkha, N., Kimchi, T., Datta, S. R., Singh, R.,
1051 Tosches, M. A., Crombach, A., & Fleischmann, A. (2023). Mammalian olfactory cortex neurons retain
1052 molecular signatures of ancestral cell types. *bioRxiv*. https://doi.org/10.1101/2023.08.13.553130

1053

Figure 1

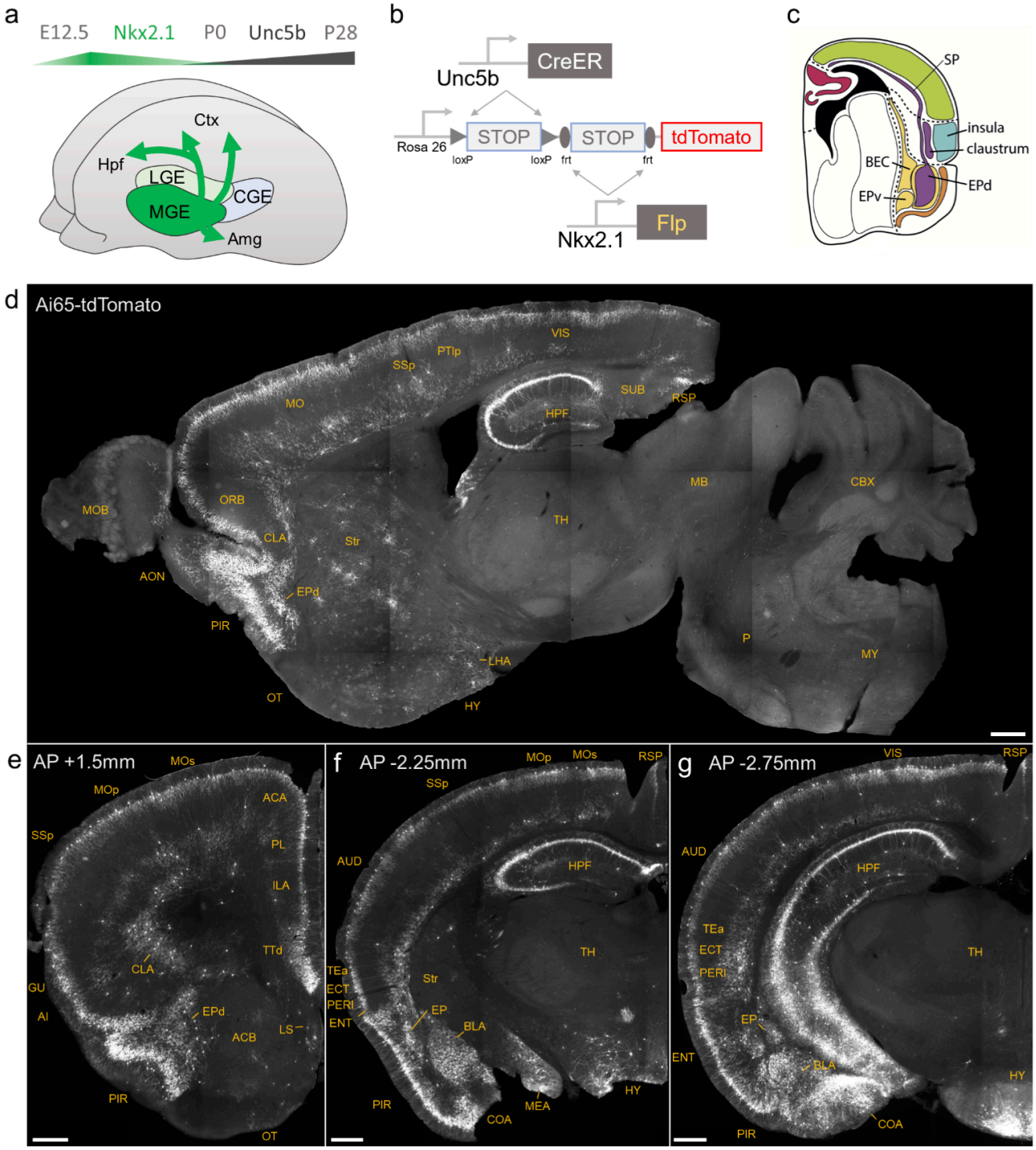
a
E12.5
Nkx2.1
P0
Unc5b
P28
Ctx
Hpf
LGE
CGE
MGE
Amg
b
CreER
Unc5b
Rosa 26
STOP
STOP
tdTomato
loxP
loxP
frt
frt
Flp
Nkx2.1
c
SP
insula
claustrum
BEC
EPd
EPv
d
Ai65-tdTomato
VIS
PTlp
SSp
SUB
RSP
MO
HPF
MB
CBX
MOB
ORB
TH
CLA
Str
AON
EPd
PIR
P
MY
LHA
OT
HY
e
AP +1.5mm
MOs
MOp
ACA
SSp
PL
ILA
TTd
CLA
GU
AI
EPd
ACB
LS
PIR
OT
f
AP -2.25mm
MOp
MOs
RSP
SSp
AUD
HPF
TH
TEa
ECT
PERI
ENT
Str
EP
BLA
HY
PIR
MEA
COA
g
AP -2.75mm
VIS
RSP
AUD
HPF
TEa
ECT
PERI
TH
EP
ENT
BLA
HY
PIR
COA

Figure 1 Supplement Figure 1

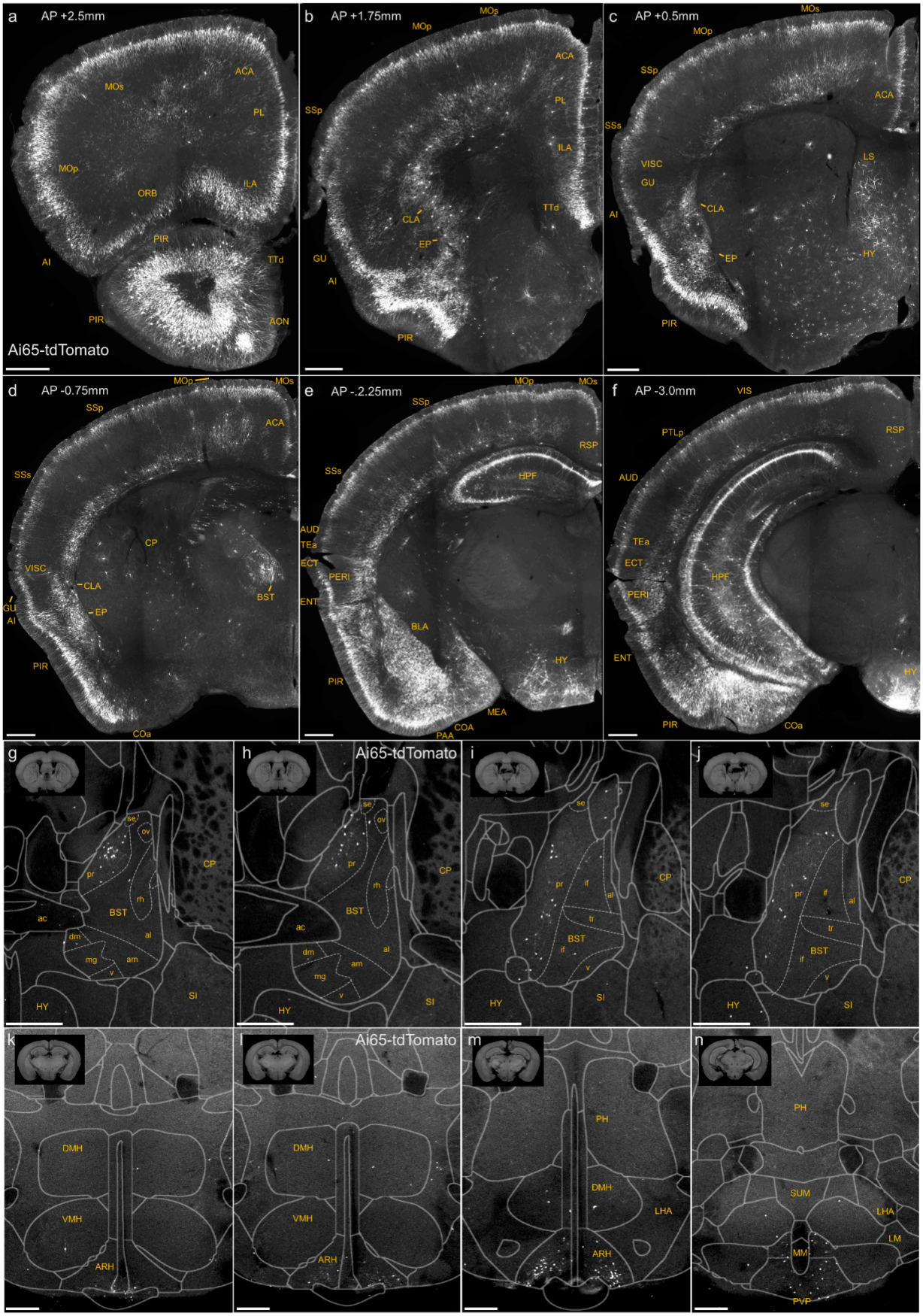

Figure 1 Supplement Figure 2

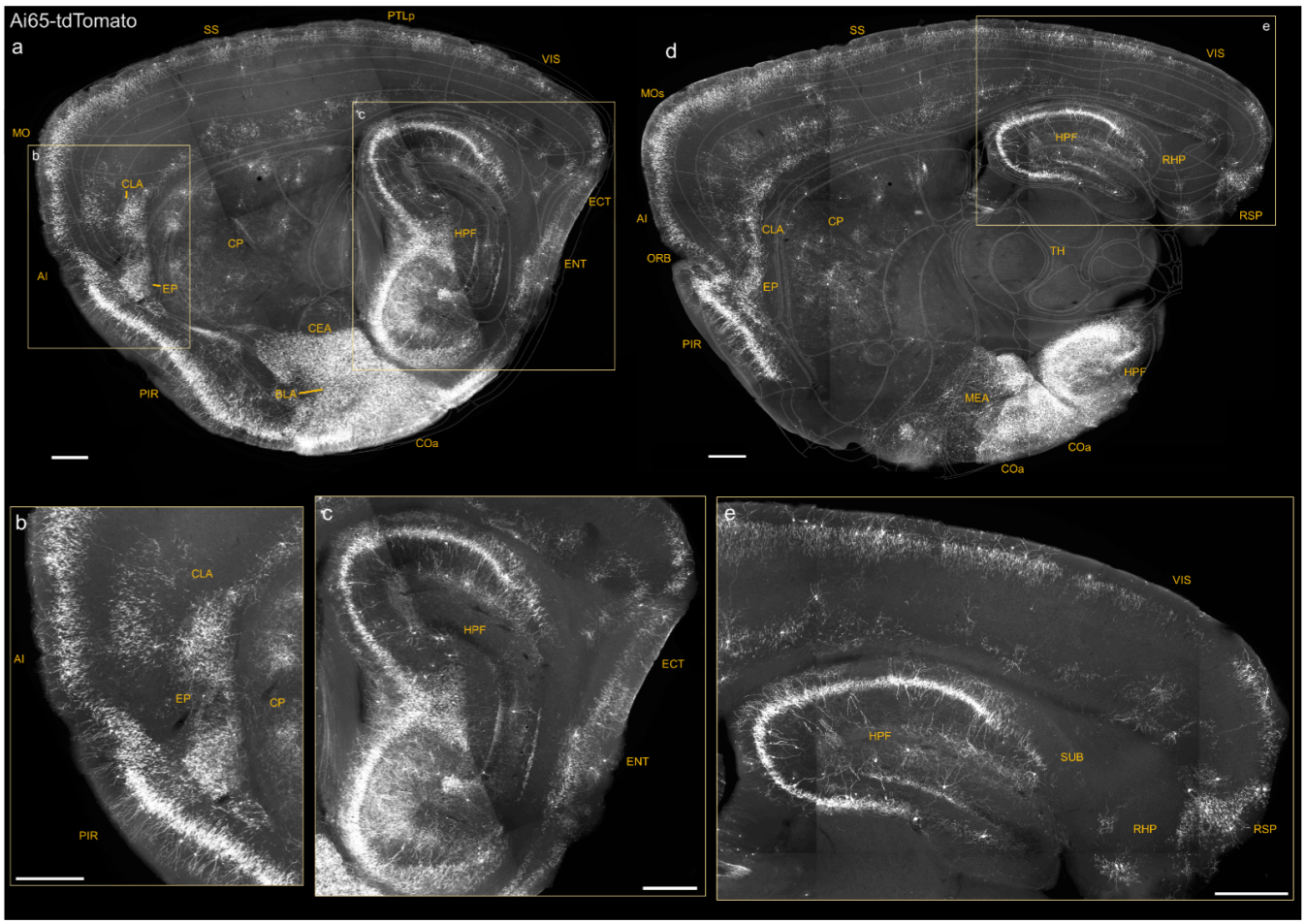

Figure 1 Supplement Figure 3

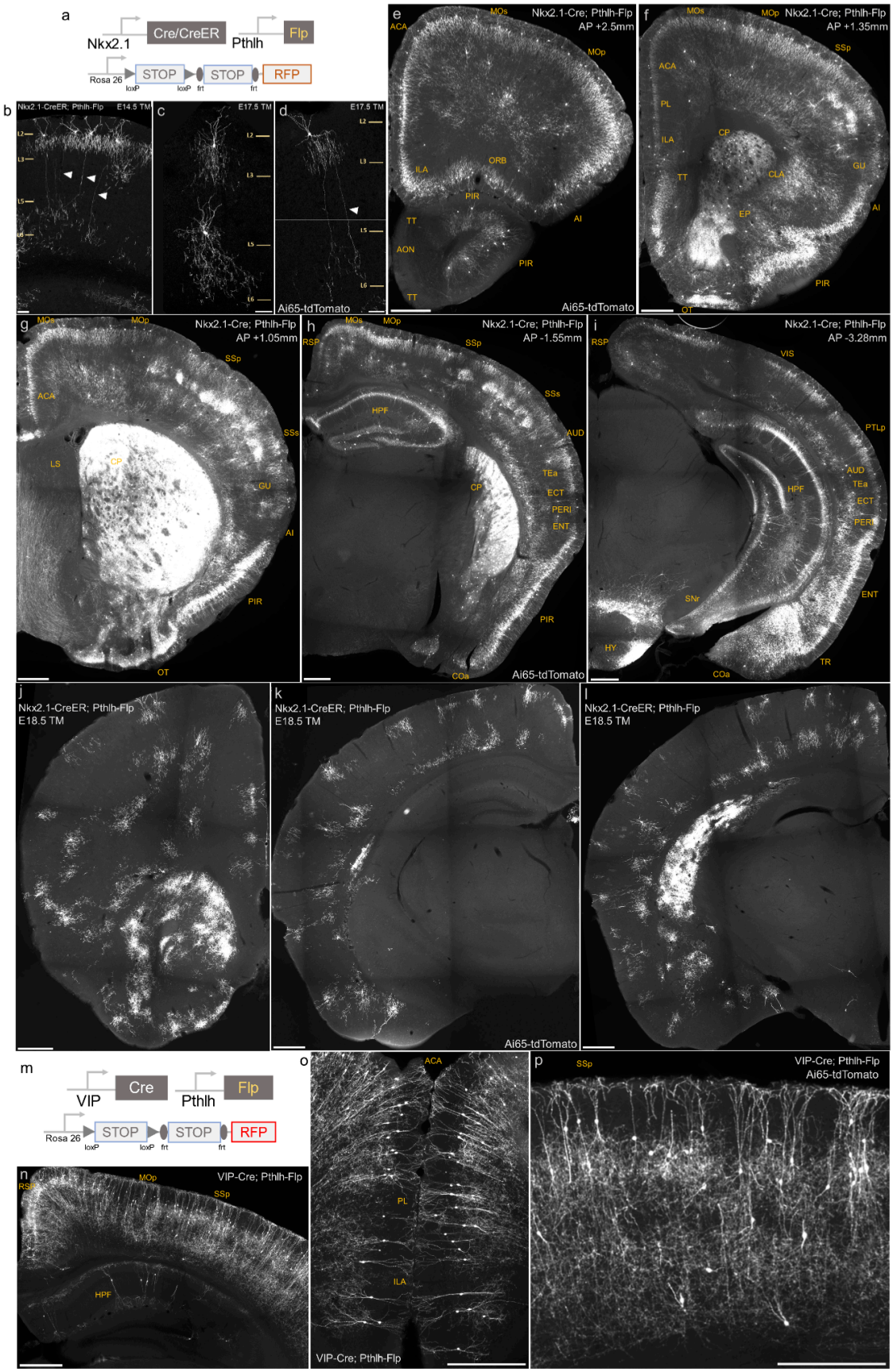

Figure 2

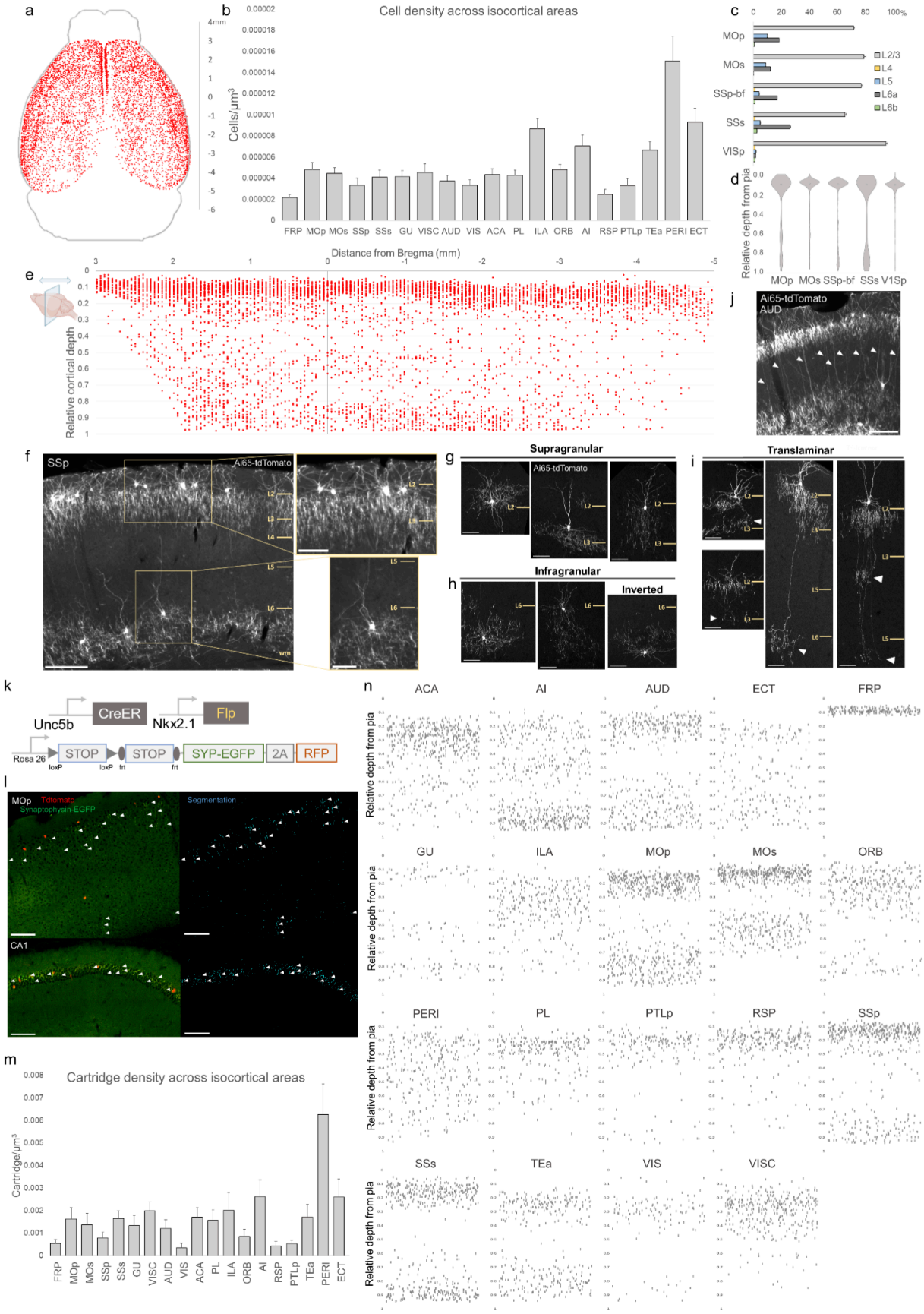
a
b
Cell density across isocortical areas
Cells/μm3
FRP MOp MOs SSp SSs GU VISC AUD VIS ACA PL ILA ORB AI RSP PTLp TEa PERI ECT
c
MOp
MOs
SSp-bf
SSs
VISp
L2/3
L4
L5
L6a
L6b
d
Relative depth from pia
MOp MOs SSp-bf SSs V1Sp
e
Distance from Bregma (mm)
Relative cortical depth
j
Ai65-tdTomato
AUD
f
SSp
Ai65-tdTomato
g
Supragranular
Ai65-tdTomato
h
Infragranular
Inverted
i
Translaminar
k
Unc5b
CreER
Nkx2.1
Flp
Rosa 26
STOP
STOP
SYP-EGFP
2A
RFP
loxP
loxP
frt
frt
l
MOp
Tdtomato
Synaptophysin-EGFP
Segmentation
CA1
m
Cartridge density across isocortical areas
Cartridge/μm3
FRP MOp MOs SSp SSs GU VISC AUD VIS ACA PL ILA ORB AI RSP PTLp TEa PERI ECT
n
ACA
AI
AUD
ECT
FRP
GU
ILA
MOp
MOs
ORB
PERI
PL
PTLp
RSP
SSp
SSs
TEa
VIS
VISC
Relative depth from pia

Figure 2 Supplement Figure 1

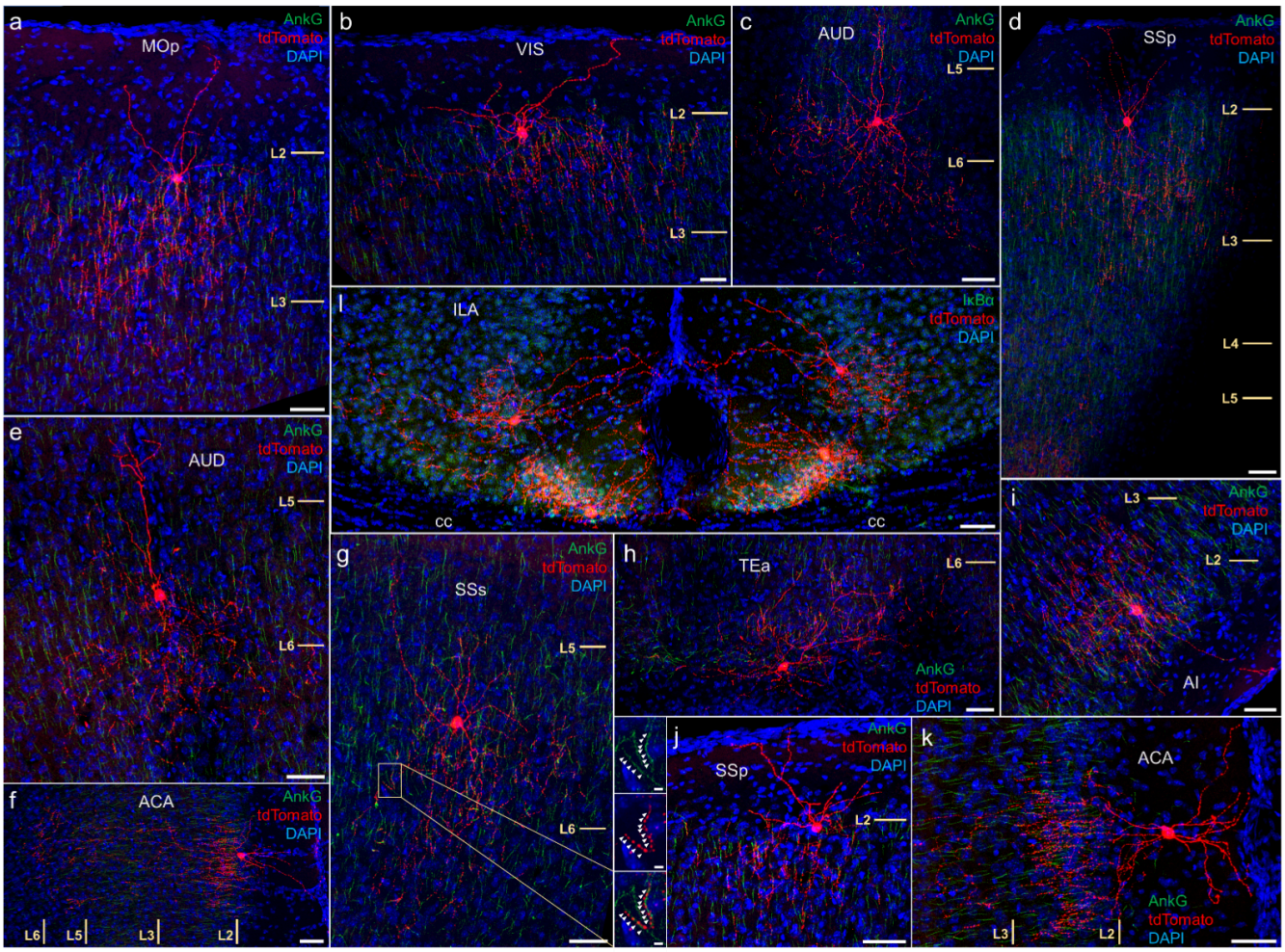

Figure 3

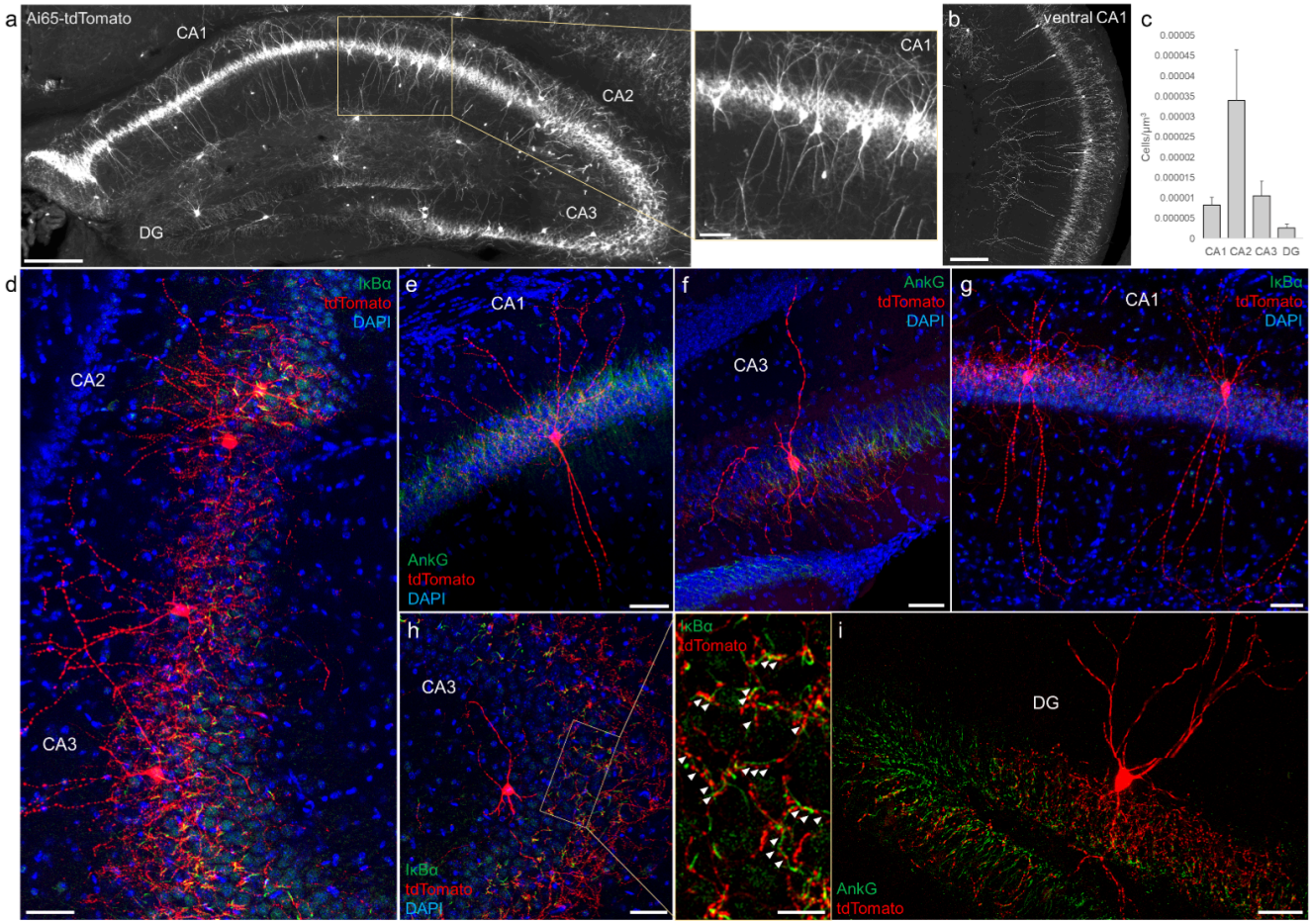
a
Ai65-tdTomato
CA1
CA2
CA3
DG
CA1
b
ventral CA1
c
Cells/µm²
0.00005
0.000045
0.00004
0.000035
0.00003
0.000025
0.00002
0.000015
0.00001
0.000005
0
CA1 CA2 CA3 DG
d
IκBα
tdTomato
DAPI
CA2
CA3
e
CA1
AnkG
tdTomato
DAPI
f
AnkG
tdTomato
DAPI
CA3
g
CA1
IκBα
tdTomato
DAPI
h
CA3
IκBα
tdTomato
DAPI
IκBα
tdTomato
i
DG
AnkG
tdTomato

Figure 4

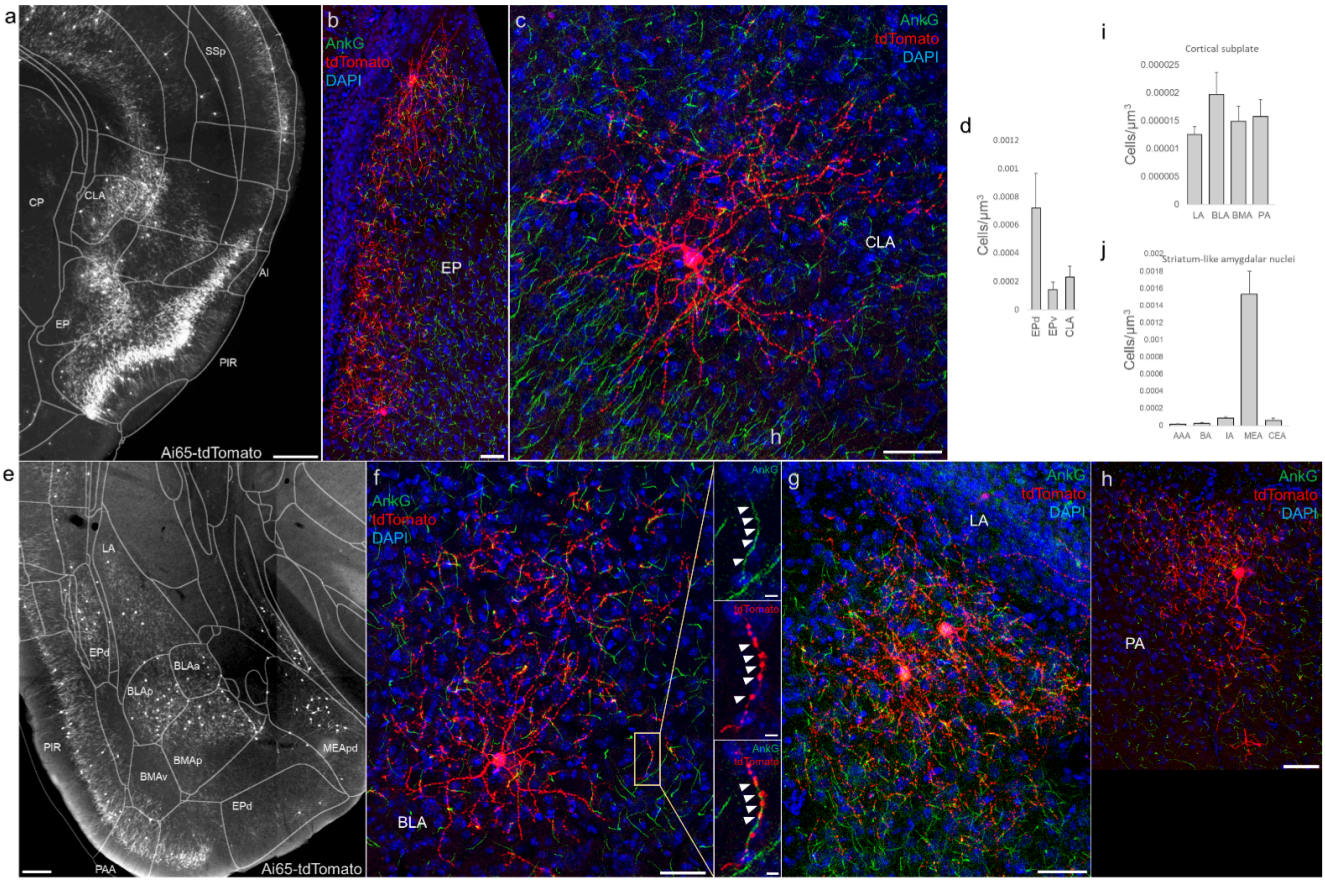
a
SSp
CP
CLA
AI
EP
PIR
Ai65-tdTomato
b
AnkG
tdTomato
DAPI
EP
c
AnkG
tdTomato
DAPI
CLA
h
d
Cells/μm3
EPd
EPv
CLA
i
Cortical subplate
Cells/μm3
LA
BLA
BMA
PA
j
Striatum-like amygdalar nuclei
Cells/μm3
AAA
BA
IA
MEA
CEA
e
LA
EPd
BLAa
BLAp
PIR
BMAp
BMAv
MEApd
EPd
PAA
Ai65-tdTomato
f
AnkG
tdTomato
DAPI
BLA
g
AnkG
tdTomato
DAPI
LA
h
AnkG
tdTomato
DAPI
PA

Figure 5

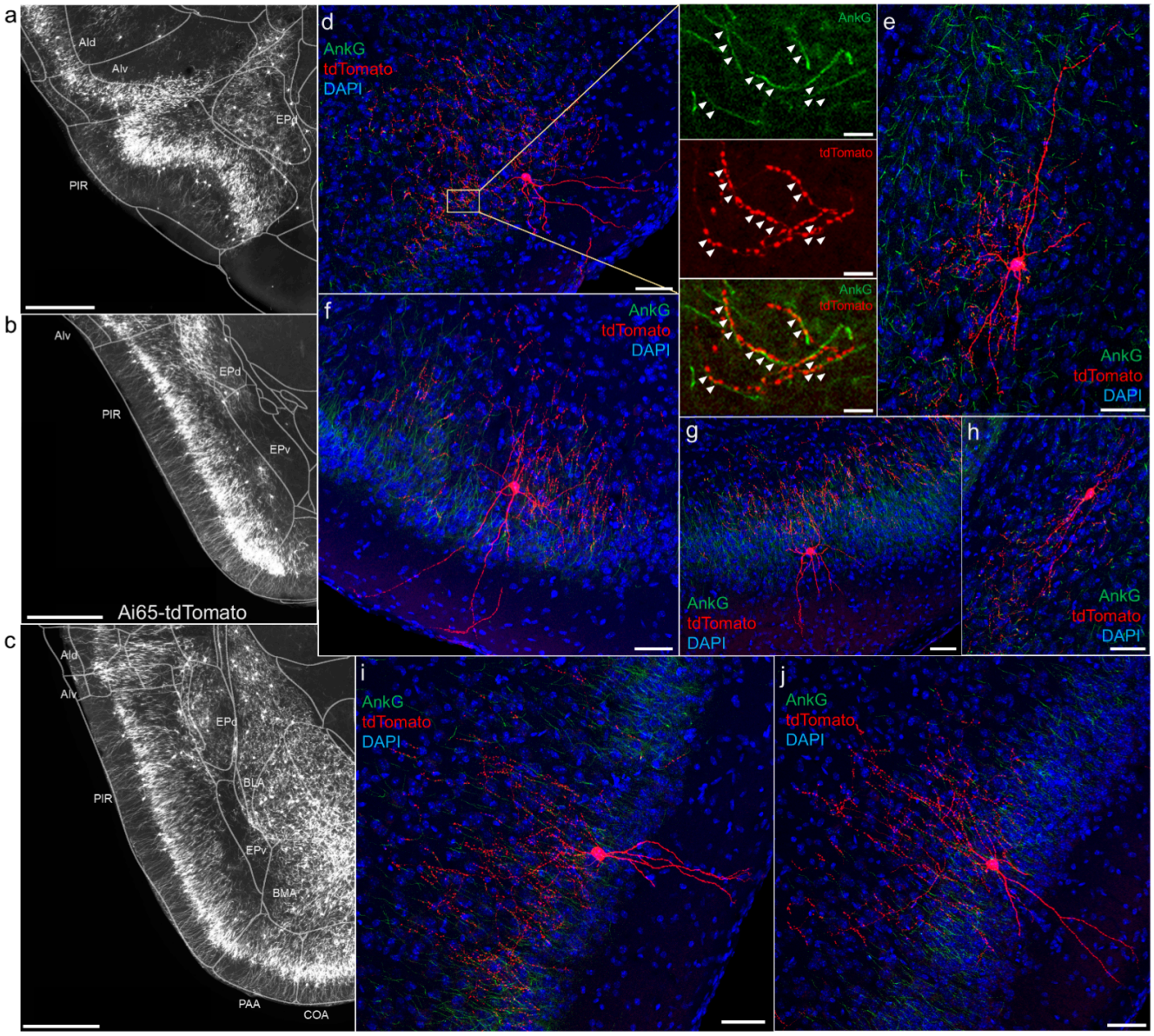
a
Ald
Alv
EPd
PIR
b
Alv
EPd
PIR
EPv
Ai65-tdTomato
c
Ald
Alv
EPd
BLA
PIR
EPv
BMA
PAA
COA
d
AnkG
tdTomato
DAPI
AnkG
tdTomato
AnkG
tdTomato
e
AnkG
tdTomato
DAPI
f
AnkG
tdTomato
DAPI
g
AnkG
tdTomato
DAPI
h
AnkG
tdTomato
DAPI
i
AnkG
tdTomato
DAPI
j
AnkG
tdTomato
DAPI

Figure 6

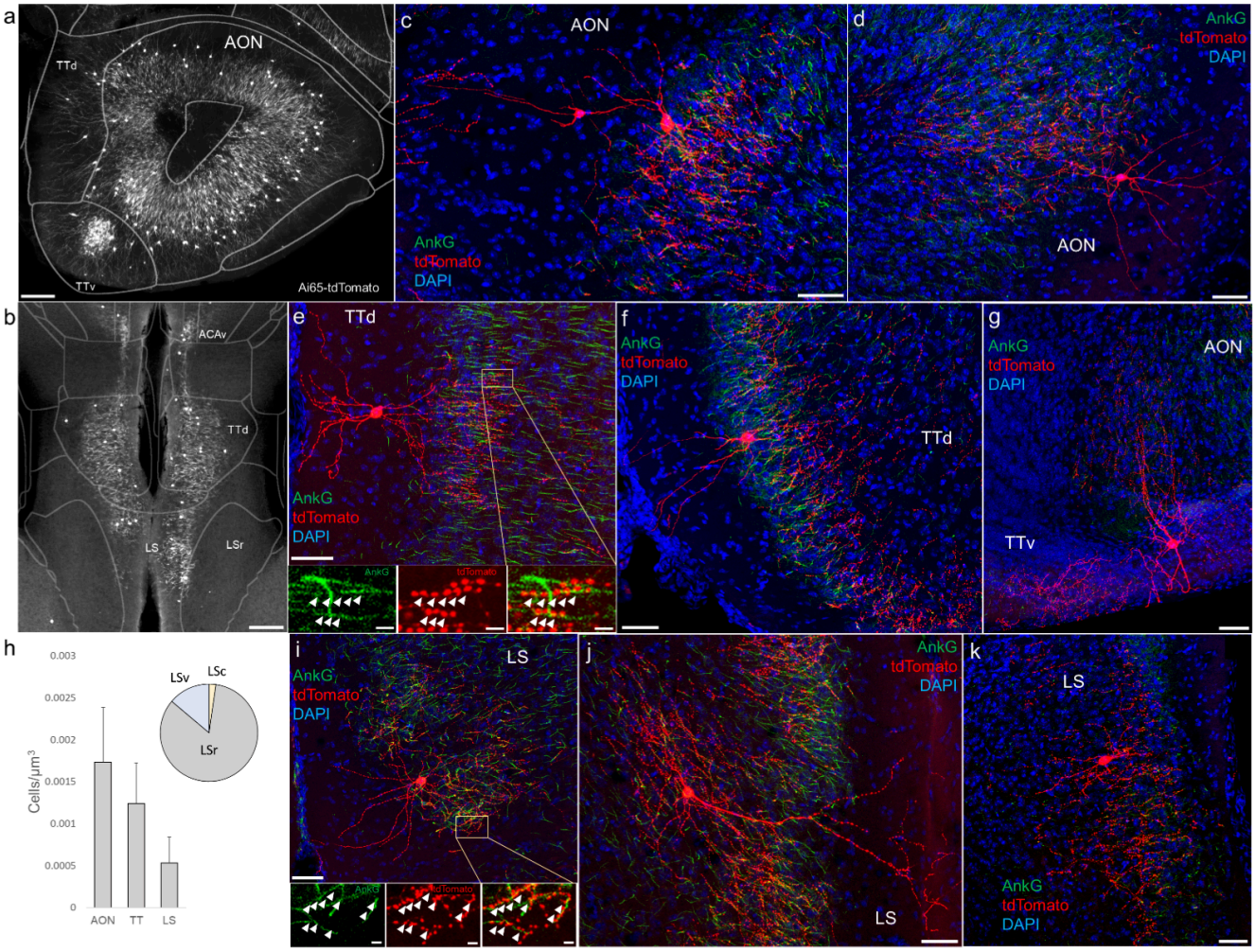
a
AON
TTd
TTv
Ai65-tdTomato
b
ACAv
TTd
LS
LSr
c
AON
AnkG
tdTomato
DAPI
d
AnkG
tdTomato
DAPI
AON
e
TTd
AnkG
tdTomato
DAPI
f
AnkG
tdTomato
DAPI
TTd
g
AnkG
tdTomato
DAPI
AON
TTv
h
Cells/μm3
0.003
0.0025
0.002
0.0015
0.001
0.0005
0
AON
TT
LS
LSv
LSc
LSr
i
LS
AnkG
tdTomato
DAPI
j
AnkG
tdTomato
DAPI
LS
k
LS
AnkG
tdTomato
DAPI

Figure 7

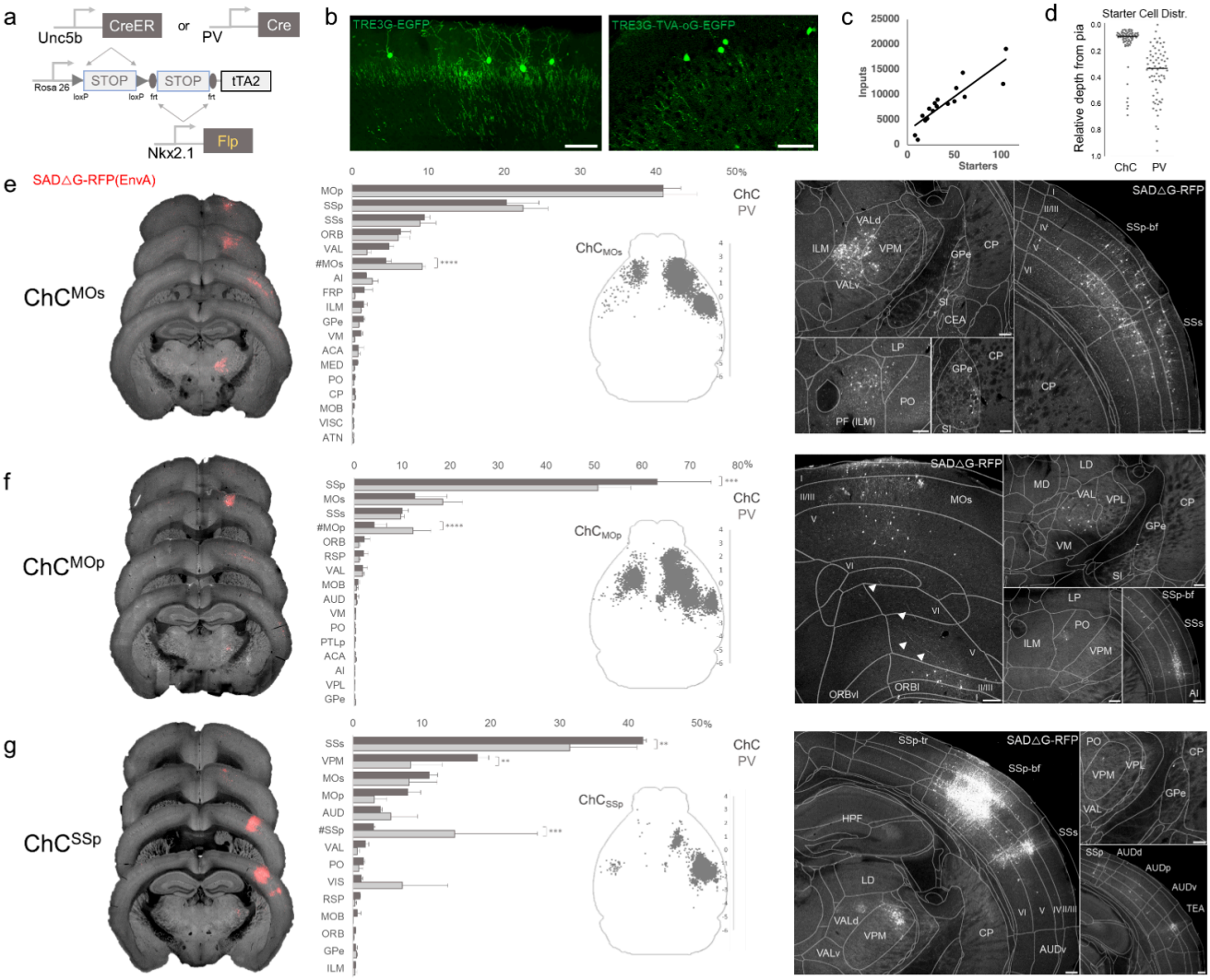
a
Unc5b
CreER
or
PV
Cre
Rosa 26
STOP
STOP
tTA2
loxP
loxP
frt
frt
Nkx2.1
Flp
b
TRE3G-EGFP
TRE3G-TVA-oG-EGFP
c
Inputs
Starters
d
Starter Cell Distr.
Relative depth from pia
ChC
PV
e
SAD△G-RFP(EnvA)
ChC^MOs
ChC
PV
ChC_MOs
SAD△G-RFP
f
ChC^MOp
ChC_MOp
g
ChC^SSp
ChC_SSp

Figure 7 Supplement Figure 1

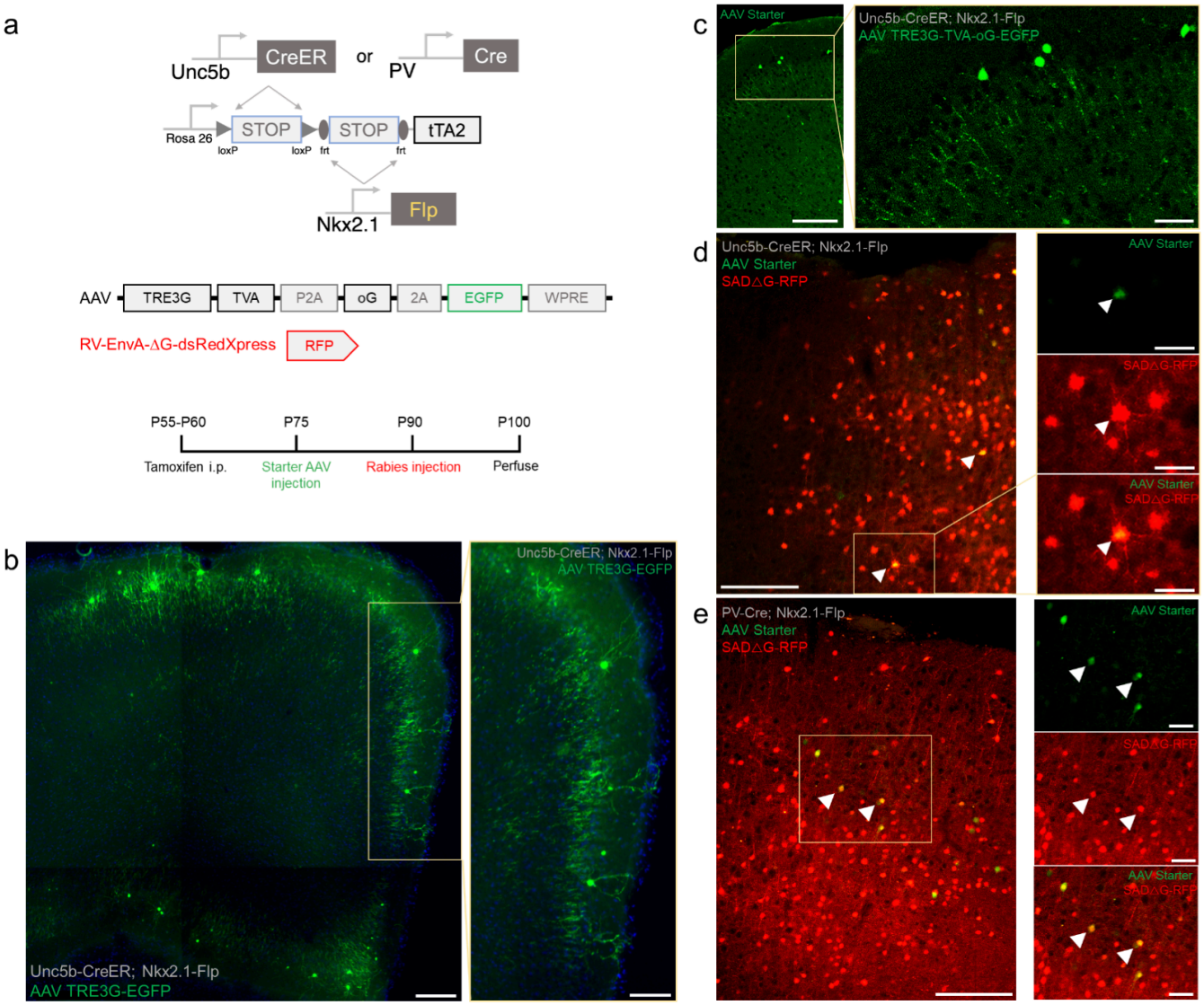

Figure 8

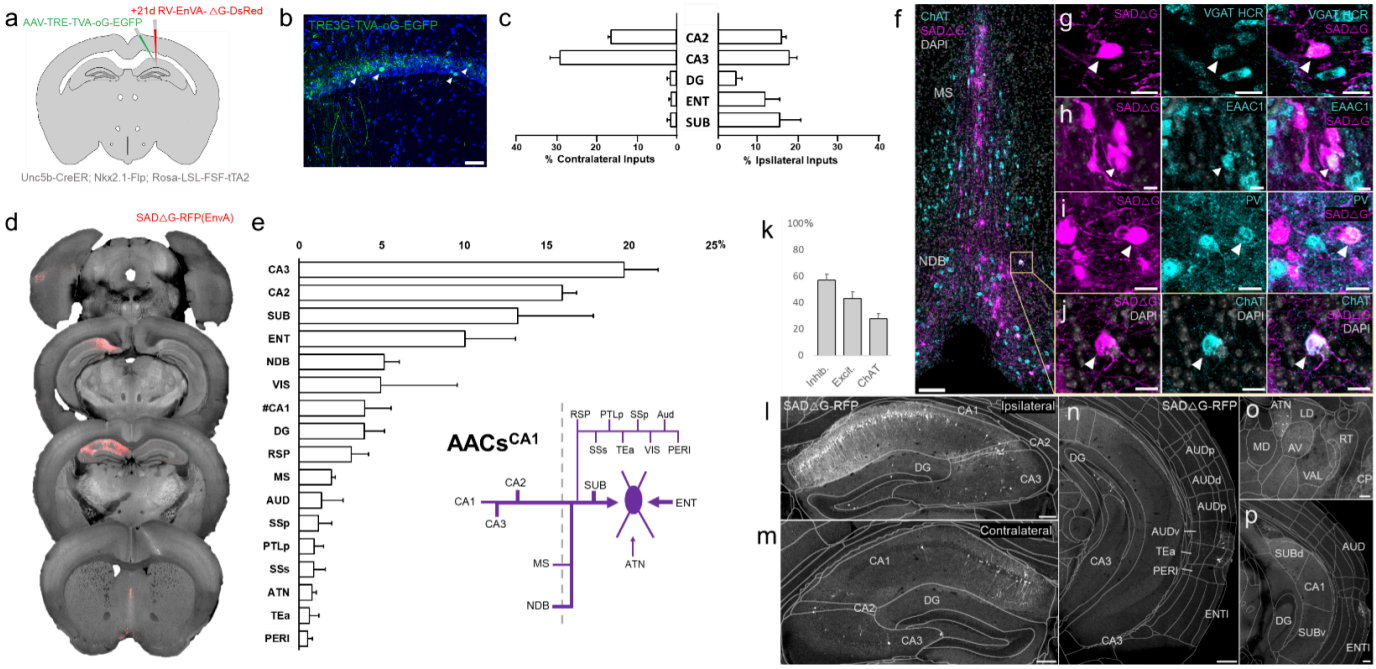
a
AAV-TRE-TVA-oG-EGFP
+21d RV-EnVA- △G-DsRed
Unc5b-CreER; Nkx2.1-Flp; Rosa-LSL-FSF-tTA2
b
TRE3G-TVA-oG-EGFP
c
CA2
CA3
DG
ENT
SUB
% Contralateral Inputs
% Ipsilateral Inputs
d
SAD△G-RFP(EnvA)
e
CA3
CA2
SUB
ENT
NDB
VIS
#CA1
DG
RSP
MS
AUD
SSp
PTLp
SSs
ATN
TEa
PERI
25%
AACs^CA1
RSP PTLp SSp Aud
SSs TEa VIS PERI
CA1
CA2
CA3
SUB
ENT
MS
NDB
ATN
f
ChAT
SAD△G
DAPI
MS
NDB
g
SAD△G
VGAT HCR
h
EAAC1
i
PV
j
ChAT
k
100%
Inhib.
Excit.
ChAT
l
SAD△G-RFP
Ipsilateral
CA1
CA2
DG
CA3
m
Contralateral
n
AUDp
AUDd
AUDv
TEa
PERI
ENTl
o
ATN
LD
RT
MD
AV
VAL
CP
p
SUBd
AUD
SUBv
ENTl

Figure 9

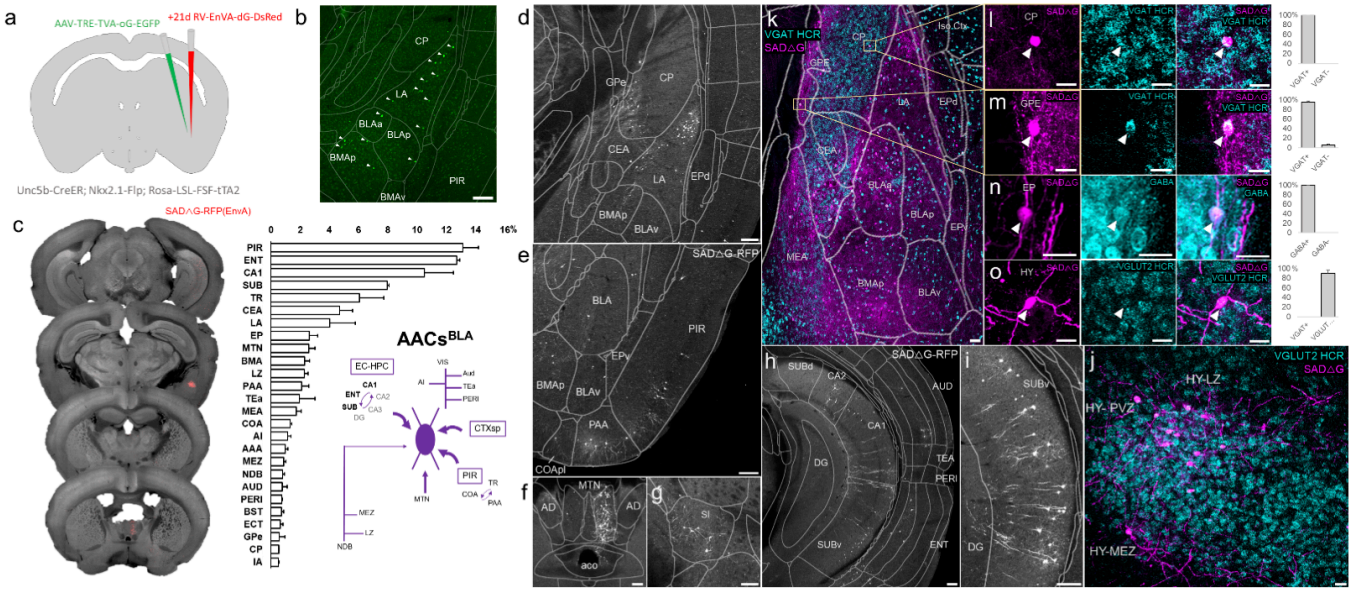

a
AAV-TRE-TVA-oG-EGFP
+21d RV-EnVA-dG-DsRed
Unc5b-CreER; Nkx2.1-Flp; Rosa-LSL-FSF-tTA2
b
CP
LA
BLAa
BLAp
BMAp
PIR
BMAv
c
SAD△G-RFP(EnvA)
0 2 4 6 8 10 12 14 16%
PIR
ENT
CA1
SUB
TR
CEA
LA
EP
MTN
BMA
LZ
PAA
TEa
MEA
COA
AI
AAA
MEZ
NDB
AUD
PERI
BST
ECT
GPe
CP
IA
AACs^BLA
EC-HPC
CTXsp
PIR
d
GPe
CP
CEA
LA
EPd
BMAp
BLAv
e
SAD△G-RFP
BLA
PIR
EPv
BMAp
BLAv
PAA
COApl
f
MTN
AD
AD
aco
g
SI
k
VGAT HCR
SAD△G
GPE
CP
LA
EPd
CEA
BLAa
BLAp
EPv
MEA
BMAp
BLAv
l
m
n
o
HY
VGAT HCR
GABA
VGLUT2 HCR
h
SUBd
CA2
AUD
CA1
DG
TEA
PERI
SUBv
ENT
i
SUBv
DG
j
VGLUT2 HCR
SAD△G
HY-LZ
HY- PVZ
HY-MEZ

Table 1. Brain-wide distribution pattern of putative AACs

Developmental origin	Brain structure	Evolutionary term	Validation
Dorsal pallium	neocortex all cortical areas entorhinal, perirhinal	isocortex	yes
Medial pallium	hippocampal formation dentate, CA1, CA2, CA3 subiculum	archicortex	yes
Lateral pallium	claustrum insular endopirifom dorsal		not yet
Ventral pallium	amygdaloid complex - BLA - CoA - MEA - BMA extended amygdala - CeA (no AACs found) - BNST (certain nuclei) olfactory cortex - piriform - endopiriform ventral [no]	paleocortex	yes
Septal neuroepithelium	-lateral and medial septum -tania tecta -AON		yes
Hypothalamo-telencephalic prosomere h1/h2	hypothalamus - arcuate nucleus - periventricular hypothalamic nucleus		not yet